Astronomy & Astrophysics manuscript no. aanda
March 20, 2024

Dynamical friction and evolution of black holes in cosmological simulations: a new implementation in `OpenGadget3`

Alice Damiano[1,2,4,5], Milena Valentini[1,2,4,5], Stefano Borgani[1,2,3,4,5], Luca Tornatore[2,5], Giuseppe Murante[2,3,5], Antonio Ragagnin[3,6,7], Cinthia Ragone-Figueroa[8,2], Klaus Dolag[9,10]

[1] Dipartimento di Fisica dell'Università di Trieste, Sez. di Astronomia, via Tiepolo 11, I-34131 Trieste, Italy
[2] INAF – Osservatorio Astronomico di Trieste, via Tiepolo 11, I-34131, Trieste, Italy
[3] IFPU, Institute for Fundamental Physics of the Universe, Via Beirut 2, 34014 Trieste, Italy
[4] INFN, Instituto Nazionale di Fisica Nucleare, Via Valerio 2, I-34127, Trieste, Italy
[5] ICSC - Italian Research Center on High Performance Computing, Big Data and Quantum Computing, via Magnanelli 2, 40033, Casalecchio di Reno, Italy
[6] INAF-Osservatorio di Astrofisica e Scienza dello Spazio di Bologna, Via Piero Gobetti 93/3, I-40129 Bologna, Italy
[7] Dipartimento di Fisica e Astronomia "Augusto Righi", Alma Mater Studiorum Università di Bologna, via Gobetti 93/2, I-40129 Bologna, Italy
[8] Instituto de Astronomía Teórica y Experimental (IATE), Consejo Nacional de Investigaciones Científicas y Técnicas de la República Argentina (CONICET), Universidad Nacional de Córdoba, Laprida 854, X5000BGR, Córdoba, Argentina
[9] Universitäts-Sternwarte München, Scheinerstr. 1, D-81679, München, Germany
[10] Max-Plank-Institut für Astrophysik, Karl-Schwarzschild Strasse 1, D-85740 Garching, Germany

March 20, 2024

ABSTRACT

Aims. We introduce a novel sub-resolution prescription to correct for the unresolved dynamical friction onto black holes (BHs) in cosmological simulations, to describe BH dynamics accurately and to overcome spurious motions induced by numerical effects.
Methods. We implement a sub-resolution prescription for the unresolved dynamical friction onto BHs in the `OpenGadget3` code. We carry out cosmological simulations of a volume of 16 cMpc^3 and zoom-ins of a galaxy group and of a galaxy cluster. The advantages of our new technique are assessed in comparison to commonly adopted methods to hamper spurious BH displacements, i.e. repositioning onto a local minimum of the gravitational potential and ad-hoc boosting of the BH particle dynamical mass. We inspect variations in BH demography in terms of offset to the host sub-halo centers, wandering population of BHs, BH-BH merger rates, and occupation fraction of sub-halos. We also analyze in detail the impact of the different prescriptions on individual events of BH interactions.
Results. The newly-introduced dynamical friction correction provides centering of BHs on host halos which is at least comparable with the other techniques, becoming gradually more effective as the redshift decreases. It predicts half as many merger events with respect to the repositioning prescription, with the advantage of being less prone to leave sub-structures without any central BH. Simulations featuring our dynamical friction prescription produce a smaller (by up to ~ 50% with respect to repositioning) population of wandering BHs and final BH masses in good agreement with observations. As for individual BH-BH interactions, our dynamical friction model captures the gradual inspiraling of orbits before the merger occurs. By contrast, the repositioning scheme, in its most classical renditions considered here, describes extremely fast mergers, while the dynamical mass misrepresents the black holes' dynamics, introducing numerical scattering between the orbiting BHs.
Conclusions. Given its performances in describing the centering of BHs within host galaxies and the orbiting of BH pair before their merging, our dynamical friction correction opens interesting applications for an accurate description of the evolution of BH demography within cosmological simulations of galaxy formation at different cosmic epochs and within different environments.

1. Introduction

Supermassive black holes (SMBHs) reside at the center of massive galaxies and are considered to affect their evolution profoundly. Numerous studies provided evidence of relations between the SMBH mass and properties of the host galaxies (e.g. Kormendy et al. 1993; Magorrian et al. 1998; Ferrarese & Merritt 2000; Gebhardt et al. 2000; Merritt & Ferrarese 2000; Ferrarese et al. 2001; Haering & Rix 2004; Gultekin et al. 2009; Graham & Driver 2007; McConnell & Ma 2013; Gaspari et al. 2019). The most widely accepted explanation is that during SMBH growth by gas accretion, a small fraction of the enormous amount of the released gravitational energy couples with the surrounding environment, regulating the galaxy star formation via various possible mechanisms (e.g. Silk & Rees 1998; Granato et al. 2004; Hopkins et al. 2005; Bower et al. 2006; Cattaneo et al. 2009; Gitti et al. 2012).

Given the influence the SMBHs play in shaping the environment where they reside, it is essential to trace their dynamics correctly. In fact, massive BHs are thought to be formed at some early epochs through mechanisms ranging from direct collapse of primodial gas clouds or as the end stage of very massive Population III stars (e.g. Bromm & Loeb 2003; Volonteri & Bellovary 2012; Mayer & Bonoli 2018), and to subsequently grow in the dense cores of galaxies. Nonetheless, recent studies have consistently shown cases of SMBHs exhibiting substantial displacements from their host galaxies (e.g. Webb et al. 2012; Menezes et al. 2014; Combes et al. 2019; Reines et al. 2020). The dynamical behaviour of SMBHs is significantly affected by the *dynamical friction* (DF) force (Chandrasekhar 1943; Binney & Tremaine 2008), exerted by the matter distribution surrounding them. This drag force in general prevents SMBHs from escaping the centers of the host galaxies, is responsible to migrate BHs

to the galaxy centers, and drives the initial stages of the merger event between two SMBHs, ultimately leading to the formation of a close pair (Begelman et al. 1980).

Cosmological simulations represent ideal tools to follow the evolution of structures given the highly non-linear astrophysical phenomena governing the interactions of baryonic matter, including gas and stars, in addition to dark matter (DM). N-body simulations describe the gravitational instability of a collisionless fluid which is sampled by a discrete set of "macro particles" (e.g. Borgani & Kravtsov 2011; Springel 2016, for reviews). For this reason, tracking orbits of single collisionless particles has little physical relevance, since what matters is their ensemble properties. A BH particle, on the other hand, is introduced in cosmological simulations as an individual collisionless particle which has a specific physical meaning and whose presence is capable to significantly impact on the global properties of the galaxy it belongs to. Unlike the surrounding macro-particles, BHs are not entities whose motion can be interpreted solely on a global scale. Instead, their motion mirrors the effective motion of an astrophysical object. The contrast between the nature of BHs in these simulations and the interpretation given to surrounding particles presents a primary conceptual obstacle when tracking the trajectories of BH particles. Specifically, scattering interactions between a BH and surrounding particles can "heat" the BH orbit. A spurious, numerical displacement of a BH from the center of the host galaxy is a major consequence of this "heating", which can eventually lead to the formation of unwanted "wandering" BHs. Furthermore, it also means a poor predicting capability of describing BH-BH merger events, ultimately leading to an incorrect description of AGN feedback, which in turn strongly affects the predictions of the simulations. For instance, Ragone-Figueroa et al. (2018) found that a better centring of the SMBH within the host galaxy in cluster simulations was the key to predict masses of the Brightest Cluster Galaxies (BCGs) in good agreement with observations, which instead were overpredicted by a factor of a few in their previous work (Ragone-Figueroa et al. 2013).

These issues stem from numerical simulations failing to recover the DF force.

Since the magnitude of DF drag depends on the interactions between BHs and the surrounding particles, any limitation in reconstructing the correct gravitational interactions at the N-body resolution level results in an inaccurate representation of this effect. In this context, our first query in this paper is whether it is feasible to introduce a correction to the gravitational acceleration provided by the N-body solver that accounts for the unresolved DF.

Instead of relying on some numerical tricks to control the dynamics of the BHs, e.g. by artificially repositioning the BHs at the position of a local minimum of the gravitational potential (Springel et al. 2005b; Di Matteo et al. 2008; Sijacki et al. 2015; Davé et al. 2019; Ragone-Figueroa et al. 2018; Bassini et al. 2019; Bahé et al. 2022), or using a boosted dynamical mass to enhance the effect of the resolved DF (DeBuhr et al. 2011; Bassini et al. 2020), some authors have already suggested addressing this problem by introducing an explicit correction for the unresolved DF (Hirschmann et al. 2014; Tremmel et al. 2015; Bird et al. 2022; Chen et al. 2022; Ma et al. 2023). For instance, Hirschmann et al. (2014) proposed the application of a DF correction given by the Chandrasekhar DF formula, which is contributed by all the particles within the half-mass radius of the substructure hosting the BH. Besides, Tremmel et al. (2015) stated that, under the hypotheses of a sufficient shallow potential surrounding the BH, only unresolved interactions within the softening length need correction. Still, Chen et al. (2022) proposed that the application the DF correction should be coupled with a boosted dynamical mass, to account for those cases in which a BH has a rather small mass, close to its value at seeding, and it is located in a poorly resolved halo. The absence of a consensus on the possibility, use and actual computation of a DF correction to improve the description of the dynamics of BHs in cosmological simulations motivates this study.

In this paper, we propose a novel implementation of DF correction, that we implement in the `OpenGadget3` code for cosmological N-body and hydrodynamical simulations. In this implementation, a correction to DF force is computed by explicitly accounting for the contributions of numerical particles whose gravitational interactions with a BH particle, as provided by the N-body solution, are directly affected by force softening. As we will extensively discuss in the following, the primary benefit of our approach is that it is less affected by the assumptions on which the derivation of the Chandrasekhar DF formula is based. In more detail, we aim to address the following questions: Does our approach provide a adequate description of the DF force acting on BHs? How does it compare against the other numerical ah-hoc prescriptions (i.e., repositioning, dynamical mass) introduced to mimic DF's effect on BH particles? To answer these questions, we will simulate a group-sized and a cluster-sized halos, with initial conditions from the `DIANOGA` set (Bonafede et al. 2011; Bassini et al. 2019, 2020), along with a cosmological box having a comoving size of 16 cMpc a side. The simulations have been carried out three times, maintaining identical settings for all parameters, except for the sub-resolution prescription governing BH dynamics: continuous repositioning on a local potential minimum, boosted dynamical mass, and our novel model to correct unresolved dynamical friction. This approach will enable us not only to focus on systems densely populated and rich in interactions, such as galaxy clusters and groups but also to undertake a statistical analysis of the BH population in a cosmological volume.

The paper is organized as follows. In Sect. 2 we present the new DF model and compare it with both previous DF corrections and numerical prescriptions to constrain the BH dynamics. In Sect. 3 we present the implementation of this model in the `OpenGadget3` code of the description of the SMBH evolution and of the ensuing AGN feedback. After introducing the details of our test simulations in Sect. 4, we present in Sect. 5 the results of our analysis of the general properties of the SMBH population. Sect. 6 will "zoom" on single BHs and merger episodes, by comparing in details the small-scale effect of our sub-resolution model of DF.

2. Dynamics of black-hole particles

Due to the finite mass and force resolution of cosmological simulations, the effect of DF exerted on a BH particle by surrounding particles is always underestimated and, in general, subject to discreteness noise. Such limitations can lead to a grossly incorrect description of the orbits of BH particles, which leads in turn to an incorrect description of the ensuing AGN feedback and of the predictions on the SMBH population.

In this section, we will present different approaches, including our new one, that have been introduced to overcome this limitation. In Sect. 2.1, we present our new description of a correction to the gravitational acceleration to account for the unresolved DF. Previous works already proposed approaches to correct DF for finite-resolution effects, and some details of our implementation revisit their arguments. For this reason, we high-

light in Sect. 2.2 the conceptual differences between our method and such previous approaches proposed in the literature. Finally, Sect. 2.2.1 and Sect. 2.2.2 describe other methods, based on ad-hoc prescriptions, to correct BH dynamics for the unresolved DF.

2.1. A new prescription for dynamical friction

To clearly describe in detail the DF correction proposed in this work, we review the basic steps of the DF expression originally derived by Chandrasekhar (1943), which holds under the assumption of specific hypotheses. The starting point is a system of two particles moving on a Keplerian orbit around each other. The velocity variation $\Delta \boldsymbol{v}_{\rm M}$ of a particle of mass M caused by the interaction with another particle of mass m and velocity $\boldsymbol{v}$ can be expressed in terms of their impact parameter b and relative velocity, $\boldsymbol{v}_0 = \boldsymbol{v} - \boldsymbol{v}_{\rm M}$, when the two particles were initially at large distance. The components of $\Delta \boldsymbol{v}_{\rm M}$ parallel and perpendicular to the direction of $\boldsymbol{v}_0$ can be expressed as (Binney & Tremaine 2008):

$$|\Delta \boldsymbol{v}_{\rm M}|_{\parallel} = \frac{2m|\boldsymbol{v}_0|}{(M+m)} \left[1 + \frac{b^2|\boldsymbol{v}_0|^4}{G^2({\rm M}+m)^2}\right]^{-1} ; \quad (1)$$

$$|\Delta \boldsymbol{v}_{\rm M}|_{\perp} = \frac{2mb|\boldsymbol{v}_0|^3}{G({\rm M}+m)^2} \left[1 + \frac{b^2|\boldsymbol{v}_0|^4}{G({\rm M}+m)^2}\right]^{-1} . \quad (2)$$

If the particle M moves in a "sea" of particles of mass m, then the DF force acting on the former arises as the sum of the contributions of the velocity variations given by eqs. (1) and (2), due to the interactions with all the surrounding particles. In the derivation by Binney & Tremaine (2008), the mass m of the "sea" particles is assumed to be the same for all such particles. Under the assumption that the distribution of particles is uniform around the BH, the perpendicular contributions of Eq. (2) sum to zero. The rate of encounters having impact parameter in the range $[b, b+db]$ is then given by: $2\pi\, b\, db\, |\Delta \boldsymbol{v}_M|_{\parallel} f(\boldsymbol{v}) d^3\boldsymbol{v}$, where $f(\boldsymbol{v})$ is the phase-space number density of stars. Integrating this rate over the impact parameter from 0 to $b_{\rm max}$ [1], we have that the DF force acting on a BH of mass M from particles having mass m and velocities in the range $(\boldsymbol{v}, \boldsymbol{v} + d^3\boldsymbol{v})$ is:

$$\left.\frac{d\boldsymbol{v}_{\rm M}}{dt}\right|_{v} = 2\pi \ln\left[1 + \Lambda(m,\boldsymbol{v})^2\right] G^2 m({\rm M}+m) f(\boldsymbol{v}) d^3\boldsymbol{v} \frac{(\boldsymbol{v}-\boldsymbol{v}_{\rm M})}{|\boldsymbol{v}-\boldsymbol{v}_{\rm M}|^3} , \quad (3)$$

where:

$$\Lambda(m,\boldsymbol{v}) = \frac{b_{\rm max}(\boldsymbol{v}-\boldsymbol{v}_{\rm M})^2}{G({\rm M}+m)} . \quad (4)$$

Here, $b_{\rm max}$ is the *maximum impact parameter*. In general, $b_{\rm max}$is interpreted as the largest distance from the target BH particle, which contains all the particles contributing to the DF exerted on the BH itself. In the above expression, we have made explicit the dependence of Λ on mass m and velocity $\boldsymbol{v}$.

The maximum allowed value of the impact parameter should in principle be set by the size of the system containing all the particles contributing to the DF exerted on a BH particle. In fact, different assumptions for the values of $b_{\rm max}$ have been introduced in the literature, all having a degree of arbitrariness. In the next section, we will provide an extended comparison between different choices. As in Tremmel et al. (2015), we will assume $b_{\rm max}$ to be given by the gravitational softening length of the BH particle, $\epsilon_{\rm BH}$, meaning that above such length, the N-body solver is assumed to provide already a correct description of DF. In the context of our simulations, the BH is surrounded by particles which trace the underlying continuous density field. Each of these particles has its mass, m_i, and its velocity $\boldsymbol{v}_{m,i}$. The phase-space number density of particles surrounding the BH can be then expressed as a sum of delta-functions, each with a mass m_i and a velocity $\boldsymbol{v}_{m,i}$:

$$f(\boldsymbol{v}) = \frac{3}{4\pi {\epsilon_{\rm BH}}^3} \sum_{i=1}^{N(<\epsilon_{\rm BH})} \delta(\boldsymbol{v} - \boldsymbol{v}_{m,i}) , \quad (5)$$

where the sum is over all the $N(<\epsilon_{\rm BH})$ particles lying at a distance from the BH smaller than its gravitational softening scale. In the simulations performed in this work, we only use DM and star particles to compute the correction to DF, while we defer to a forthcoming analysis the inclusion of gas particles (see for example Dubois et al. 2014). Using Eqs. (3) and (5), we can then derive the total DF force term, by integrating over the surrounding particles' velocities:

$$\frac{d\boldsymbol{v}_{\rm M}}{dt} = \frac{3}{2{\epsilon_{\rm BH}}^3} \sum_{i=1}^{N(\epsilon)} \ln\left[1 + \Lambda(m_i)^2\right] m_i({\rm M}+m_i) \frac{(\boldsymbol{v}_{m,i} - \boldsymbol{v}_{\rm M})}{|\boldsymbol{v}_{m,i} - \boldsymbol{v}_{\rm M}|^3} . \quad (6)$$

The gravitational acceleration of the BH is then corrected by the DF acceleration $\boldsymbol{a}_{\rm df}$ given by Eq. (6), so that the total acceleration acting on a single BH particle is:

$$\boldsymbol{a}_{\rm BH} = \boldsymbol{a}_{\rm g} + \boldsymbol{a}_{\rm df} . \quad (7)$$

where $\boldsymbol{a}_{\rm g}$ is the acceleration provided by the N-body solver. It is important to remark that the DF correction hence obtained is a contribution correcting for the softened interactions between the BH and the surrounding particles, but not for the absence of information on the sub-softening structure of phase-space. This approach for the computation of the DF correction presents some advantages with respect to the models proposed in the literature. We will discuss this in the next section, providing an overview of the implementations adopted nowadays and underlining their differences with our approach.

2.2. Previous approaches

Correcting the unresolved DF force acting on BH particles using a physically motivated approach instead of resorting to ad-hoc prescriptions is clearly highly desirable. This is the reason why, the implementation of a correction of the DF force acting on BH particles, based on the original derivation by Chandrasekhar (1943), has been explored in various studies since the very first implementations (e.g., Hirschmann et al. 2014, Tremmel et al. 2015). A common aspect of all such approaches is that they start from Eq. (3), and implicitly assume that the BH is surrounded by a homogeneous and infinite distribution of particles all having the same mass. However, different approaches make different assumptions of the physical size of the region where to correct for the unresolved DF, i.e. on the actual value of $b_{\rm max}$. For instance, in the work by Hirschmann et al. (2014), $b_{\rm max}$ is defined as the typical size of the system hosting the BH and, as such, it is set to the half-mass radius of the sub-halo[2]. On the

[1] In principle this integration should be performed from a minimum value of the impact parameter equal to the Schwarzschild radius of the BH. It is unnecessary to consider this contribution to derive an expression for our DF correction. Therefore, we will assume the minimum value of b to be zero.

[2] This parametrization required an on-the-fly execution of the `SubFind` algorithm (Springel et al. 2001a; Dolag et al. 2009) to identify the substructures hosting the BHs and to compute their half-mass radius.

other hand, Tremmel et al. (2015) argued that DF is correctly computed by the N-body solver at scales larger than the gravitational softening length of the BH, $\epsilon_{\rm BH}$. Accordingly, a correction term to the DF should be added only on scales smaller than $\epsilon_{\rm BH}$, so that $b_{\rm max} = \epsilon_{\rm BH}$. In line with this approach, Pfister et al. (2019) accounted for the DF force from particles within a sphere centered on the BH position and with radius which is a multiple of the adaptive grid mesh size on which the gravitational force is computed (Teyssier 2002). Finally, the DF model recently presented by Chen et al. (2022) and Bird et al. (2022) assumes a constant value of $b_{max} = 10h^{-1}$ckpc and 20 kpc, respectively. As for the velocity distribution function of the sea of particles around the BH, Hirschmann et al. (2014), Chen et al. (2022) and Bird et al. (2022) adopt the same standard hypothesis, originally formulated by Binney & Tremaine (2008), of a local Maxwellian velocity distribution. Under the further hypothesis that $M_{\rm BH} \gg m$, where m is the mass of the particles around the BH, the dynamical friction force $\boldsymbol{F}_{\rm DF}$ can be cast in the form

$$\boldsymbol{F}_{\rm DF} = -4\pi\rho\left(\frac{G\mathrm{M_{BH}}}{v_{\rm BH}}\right)^2 \mathrm{F}(x)\ln(\Lambda)\widehat{v}_{\rm BH}\,. \tag{8}$$

Here ρ is the smoothed density at the position of the BH, contributed by stellar and DM particles, using the BH smoothing length. Furthermore, $\widehat{v}_{\rm BH}$ is the versor of the BH velocity relative to the "sea" of surrounding particles, while

$$\mathrm{F}(x) = \mathrm{erf}(x) - \frac{2x}{\sqrt{\pi}}e^{-x^2} \;\;;\;\; x = \frac{v_{\rm BH}}{\sigma_v}, \tag{9}$$

with σ_v the velocity dispersion of the surrounding particles. We will assume that stars and DM particles exert a dynamical friction force on the BHs. Ostriker (1999) computed the contribution to DF from gas, lately included in simulations as an additional numerical corrective term by Chen et al. (2022). However, in their analysis, Chen et al. (2022) found that the DF correction is in fact dominated by the collisionless component.

Rather than assuming a specific expression for the velocity distribution function of the particles around a BH, Tremmel et al. (2015) proposed to incorporate the mass m of the surrounding particles within the integral over velocities, thus moving the uncertainty on the velocity distribution function to an uncertainty on the mass density of the surrounding particles. The approach by Tremmel et al. (2015) has been then applied also in Bellovary et al. (2018). They found that the effect of DF correction is efficient for BHs having a mass at least three times larger than that of the surrounding particles. This result justifies the choice made by Chen et al. (2022) to include both a DF correction and a boosted dynamical mass for BH particles (see Sect. 2.2.2 below).

Finally, a scheme that stands out from the others is the one proposed by Ma et al. (2023). In their approach, a discrete N-body correction, similar to the one proposed in this paper, is taken into account, but still acting only on scales above the gravitational force resolution of simulations. Differently from such an approach, the model that we described in Sect. 2.1 explicitly intends to correct for the interactions that take place below the BH softening scale which, by definition, are not correctly described by the N-body solver. In our approach, without any a-priori assumption on the velocity dispersion of the surrounding particles, BH motion correction arises from summing over the single contributions of scattering events taking place below the softening length. Consequently, each scattering particle will contribute to the correction with its specific velocity and mass. In this sense, our approach relaxes the approximation of negligible mass of the particles belonging to the "sea", which is needed to derive Eq. (8).

2.2.1. Repositioning BH particles

Among the major issues encountered when introducing BH particles in N-body simulations is that they can escape from the centers of the host galaxies. One of the most widely used methods to avoid this consists of repositioning, at each time step, the BH particle at the position of the most bound particle among its *neighbours*. Different implementations of this method feature different choices for the search radius. Moreover, such alternative implementations often adopt additional constrains (e.g., on their relative velocity) for the selection of the neighbour particle on which to relocate the BH. In this way, the BH particle is generally forced to remain at the centre of its host sub-halo (see e.g. Di Matteo et al. 2008; Booth & Schaye 2009; Vogelsberger et al. 2013; Sijacki et al. 2015; Schaye et al. 2014; Pillepich et al. 2017; Ragone-Figueroa et al. 2018; Bahé et al. 2022).

As pointed out by Tremmel et al. (2015), this method may have major shortcomings during mergers or high-speed close encounters between galaxies. During a close encounter between two galaxies, one of the two BHs may select the most bound neighbour particle as a particle belonging to the other galaxy. In this case, at the next time step the BH is suddenly and unphysically relocated to the neighbouring galaxy, thus leaving its original host galaxy without a central BH. In addition, this BH, which has typically moved to an outer region of the galaxy, will be quickly repositioned closer to the centre of the new host galaxy, where another BH is located, within a few time steps. In this way, BH-BH mergers will become faster and more frequent.

To prevent the occurrence of these spurious behaviours, different definitions of the neighbours, over which to search for the most bound particle, have been employed. The original radius was set as the SPH smoothing radius of the BH particle, or some kernel radius associated to a different hydro solver (e.g. Di Matteo et al. 2008; Vogelsberger et al. 2013; Davé et al. 2019). Other authors preferred to search the most bound particle within the BH gravitational softening or a small multiple of it (e.g. Booth & Schaye 2009; Schaye et al. 2014; Ragone-Figueroa et al. 2018) because the smoothing length can be much larger, thus exacerbating the problem mentioned above.

A further condition usually introduced to search for the most bound particle is that its velocity relative to the BH has to be smaller than a threshold in the attempt to ensure that it belongs to the same galaxy. The most commonly used threshold is a fraction of the local sound speed, as originally introduced by Di Matteo et al. (2008). However, Ragone-Figueroa et al. (2018) found that this criterion is not effective, besides having a not-so-clear physical basis (see also Bahé et al. 2022). Their results improved by imposing a maximum velocity of the order of the typical motions of particles within galaxies, namely 100-200 km/s. These values and the smaller search radius limited the unphysical transfer of a BH to another galaxy in their zoom-in massive cluster simulations since the typical orbital velocities of galaxies in clusters are much larger. The choice of this limiting relative velocity becomes a parameter that should be tuned to the typical merger events and the resolution of the simulation.

In the simulations presented in this work, we adopted a version of the repositioning close to the original implementation, where the most bound neighbour particle is selected within the SPH smoothing length, provided that its relative velocity is smaller than 25 % of the local sound speed.

We emphasize that the main purpose of our analysis is to highlight the potential dangers in the use of an ad-hoc repositioning model.

2.2.2. Boosting the dynamical mass

An alternative approach to account for the limited mass resolution when the mass of the BH particles is close to its seeding mass is to increase the BH dynamical mass at seeding artificially. In this approach, once seeded, two different masses are assigned to the BH: the *real* mass, m_r, which grows continuously by the Eddington-limited Bondi-like prescription (see Sect. 3.2.2 below), and the *dynamical* mass, m_d, which enters in the computation of gravitational force. At seeding, the latter is set at a relatively large value, typically equal to the mass of DM particles, while the former is a few orders of magnitude smaller. As long as $m_r < m_d$, the value of m_d does not increase by gas accretion, which only affects the value of m_r. Once $m_r \geq m_d$, the real mass increases in a continuous way, while the dynamical mass increases according to a stochastic prescription for the swallowing of neighbour gas particles (e.g. Springel et al. 2005a). From then on, the two masses remain similar, differing only because of the stochastic swallowing of gas particles.

This artificial boost of the BH dynamical mass at seeding is intended to amplify the effect of the numerically resolved DF, eventually preventing the BH from escaping the host halo soon after it is seeded.

Clearly, also this method is prone to spurious effects. For instance, Tremmel et al. (2015) pointed out that initializing the BH mass to a value hundreds of times higher than its real value can affect the mass of the host galaxy, thus unavoidably impacting on its subsequent evolution.

In this Section, we reviewed the most commonly used techniques to deal with BH dynamics, mainly to provide a background to the simulations presented in this work. We refer the reader to Di Matteo (2023) for a more comprehensive discussion.

3. Super-massive Black Holes in cosmological simulations

In this section we discuss the description of SMBH evolution and of the ensuing AGN feedback in our simulations. In Sect. 3.1 we will briefly give an overview of the `OpenGadget3` code, within which we implemented our model to correct for unresolved DF. Given the finite force and mass resolution of cosmological simulations, sub-resolution models are needed to describe the processes of birth, accretion, and feedback of SMBHs. Furthermore, the merger events between BH pairs cannot be followed down to the final inspiraling of their orbits. Therefore, we need to include also some criteria to establish when to merge two BHs. In Sect. 3.2 we review the approach to treat BHs in cosmological simulations, by focusing on the seeding criterion (Sect. 3.2.1), on gas accretion (Sect. 3.2.2), and on the conditions allowing BH-BH mergers (Sect. 3.2.3).

3.1. The `OpenGadget3` simulation code

Our simulations are based on the `OpenGadget3` code (Dolag et al., in preparation; see also Groth et al. 2023), which represents an evolution of the `GADGET-3` code (which, in turn, is an improvement of the previous `GADGET-2` code by Springel 2005). `OpenGadget3` solves gravity with the Tree-PM method (see also Ragagnin et al. 2016). In the simulations presented here, hydrodynamics is described by the SPH formulation presented by Beck et al. (2016), which overcomes several of the limitations of the original SPH formulation of GADGET-3.

`OpenGadget3` is parallelized using a hybrid MPI/OpenMP/OpenACC scheme (Ragagnin et al. 2020). Adopting a limited number of MPI tasks per node allows us to reduce the "communication surface", while efficiently using OpenMP inside a single shared-memory node. Load-balancing is achieved using a domain decomposition based on a space-filling Peano-Hilbert curve, whose fragmentation into segments (each assigned to an MPI task) guarantees a very good computational balance, at the expense of some memory imbalance (Springel et al. 2005b).

`OpenGadget3` includes a sub-resolution description of a range of astrophysical processes relevant for the simulations presented here: metallicity-dependent radiative cooling (e.g. Wiersma et al. 2009), an effective model for star formation from a sub-resolution description of the multi-phase structure of the interstellar medium (Springel & Hernquist 2003), a model for stellar evolution and chemical enrichment from AGB stars and type-Ia and II supernovae (Tornatore et al. 2007; Bassini et al. 2020), and a model to follow the evolution of SMBHs and the ensuing AGN feedback (see below for details). As for the latter, we remind that the aim of this paper is to present an improved implementation of a sub-resolution description of the effect of DF on the dynamics of BH particles (see Sect. 2 for details).

3.2. Black holes in cosmological simulations

3.2.1. Black hole seeding

In our simulations, BHs are described by collisionless sink particles which are initially seeded within a halo hosting a "bona fide" galaxy. The halo is identified through a Friend-of-Friend (FoF) algorithm (with linking length equal to 0.2 times the mean separation of DM particles). For a BH particle to be seeded, we require the host halo to fulfill few conditions, so as to guarantee that it is well resolved and that star formation already took place within it. Following Hirschmann et al. (2014), we added to the halo mass threshold criterion introduced by Springel et al. (2005b) additional conditions for star and gas fraction of the halo.

In detail, in the simulations presented in this work, the following seeding conditions must all be met: *(i)* the DM mass of the halo exceeds the value of 6.94×10^{10} $M_\odot$; *(ii)* the stellar mass is at least 2 per cent of the total mass and 0.05 times the DM mass of the halo; *(iii)* the gas mass reaches a value of 10 per cent of the stellar mass; *(vi)* the halo does not contain any other BH particle. If a halo fulfils these conditions, the most bound star particle of the halo is converted into a BH. The mass of a BH particle at seeding, $M_{\rm BH,seed}$, is not fixed, but scales with the amount of stars in the FoF group according to:

$$M_{\rm BH,seed} = M_0 \, \frac{M_{*,\rm h}}{f_* \, M_{\rm DM,seed}} \, , \tag{10}$$

where $M_{*,\rm h}$ is the stellar mass assigned to a FoF halo, f_* and $M_{\rm DM,seed}$ are the input parameters for the fraction of stellar mass and the minimum DM mass for a FoF halo where to seed a BH, respectively. As for M_0, it is the minimum seeding mass of a BH particle, when the seeding conditions are just met. In the simulations presented in this work, the mass of star particles (see Sect.4 and Table 1) is larger than M_0. Therefore, the assumption that the BH mass is larger than the one of the surrounding objects, on which the derivation of the Chandrasekhar DF formula is based, is not met at seeding due to limited mass resolution, and for the above condition to hold BHs need to grow by a large factor. Therefore, it is not surprising that, despite the initial BH

position is at the location of the most bound particle, two-body scatterings with neighboring particles can easily cause the BH to be scattered outside its host galaxy.

3.2.2. Gas accretion onto BHs

During its evolution, the mass of a BH increases through two channels: accretion of surrounding gas and merging with other BHs. As for the former, we adopt the accretion model originally implemented by Springel et al. (2005b). BH accretion rate is calculated according to Bondi-Hoyle formula (Hoyle & Lyttleton 1939; Bondi & Hoyle 1944; Bondi 1952) as

$$\dot{M}_{\rm Bondi} = \frac{4\pi^2 M_{\rm BH}^2 \alpha \rho}{(c_s^2 + v^2)^{3/2}}\,, \tag{11}$$

where ρ and c_s are the density and the sound speed of the surrounding gas computed at the position of the BH particle, v is the relative velocity of the BH with respect to the surrounding gas particles, and α is a "boost" factor introduced to account for the limited resolution with which gas density in the surroundings of the BHs is reconstructed. Following Steinborn et al. (2015), we distinguish between accretion from the hot ($T > 10^5$ K) and the cold gas ($T < 10^5$ K), using $\alpha = 10$ and $\alpha = 100$ respectively for the hot and the cold gas.

The accretion is always limited to the Eddington accretion rate,

$$\dot{M}_{\rm Edd} = \frac{4\pi M_{\rm BH} m_p}{\eta_r \sigma_T c}\,, \tag{12}$$

where m_p is the proton mass, σ_T is the Thompson cross-section. The parameter η_r is the *radiative efficiency* and represents the fraction of the accreted rest-mass energy which is converted in radiation (Novikov & Thorne 1973; Noble et al. 2011). In our simulations, we use $\eta_r = 0.1$. In addition, we allowed the black hole to swallow gas particles via stochastic accretion, as originally proposed by Springel et al. (2005b). Following Fabjan et al. (2010), gas particles are not swallowed entirely, but are sliced into three parts, so as to have a more continuous description of stochastic accretion. In this way, we can assign to each BH two masses that in general slightly differ: a "true" mass, which grows in a continuous way according to the above Eddington-limited Bondi-like accretion model, and a dynamical mass, which is varied each time that a portion of a gas particle is stochastically selected for the swallowing.

3.2.3. Mergers

The finite force resolution set by the gravitational softening sets the scale below which gravitational interactions, including mergers between BHs, cannot be properly followed. The simplest criterion for defining when a BH-BH merging event occurs is to impose a limiting BH-BH distance, $d_{\rm merg}$, below which the two BHs could immediately merge. In our simulations, we adopt a value of $d_{\rm merg} = 5 \cdot \epsilon_{\rm BH}$. However, during fly-by encounters between galaxies, it could happen that this criterion produces an unwanted behaviour, with the two BHs forced to merge, even if their relative velocities are large enough to make them gravitationally unbound. To circumvent this, we follow Di Matteo et al. (2008) to include in our simulations the following criterion, that should guarantee that the BHs are actually gravitationally bound:

$$\frac{|\Phi_{\rm BH_1} - \Phi_{\rm BH_2}|}{a} < 0.5 \cdot c_s^2 - v_{\rm rel}^2\,, \tag{13}$$

where $\Phi_{\rm BH_1}, \Phi_{\rm BH_2}$ are the values of the gravitational potential at the positions of the two merging black holes, c_s is the local sound speed, $v_{\rm rel}$ their relative velocity and a is the scale factor, normalized to unity at redshift $z = 0$. During a merger event involving two BHs, the BH having a lower value of the potential swallows the other BH. Consequently, after the merger, the surviving BH retains its original position, while its mass increases by the mass of the swallowed BH.

3.2.4. Feedback energy

As a BH accretes gas, it injects energy in the surrounding region and a fraction of the energy radiated during gas accretion is thermally coupled in the form of feedback energy to the surrounding medium (Wurster & Thacker 2013, for an extensive comparison of different implementations of AGN feedback in simulations). Within the simulations presented in this work, we consider a purely thermal mechanism of feedback, whose energy rate is calculated according to

$$\dot{E} = \eta_r \eta_f \dot{M}_{\rm BH} c^2\,. \tag{14}$$

In the above expression, $\dot{M}_{\rm BH} = \min(\dot{M}_{\rm Bondi}, \dot{M}_{\rm Edd})$ is the BH mass accretion rate, and η_f is the fraction of the radiated energy that is thermally coupled to the surrounding gas. Furthermore, we emulate a transition between the *radio* and *quasar* mode of BH feedback by varying the parameter η_f, as described by Sijacki & Springel (2006) and Fabjan et al. (2010). Whenever the accretion rate of the BH is one-hundredth of the Eddington limit, we increased the fraction of energy thermally coupled with the surrounding gas by a factor of four. We adopt a value of $\eta_f = 0.05$ during the quasar mode, increasing to $\eta_f = 0.2$ during the radio mode.

For the seek of clarity, we summarize in Table 1 the information on the force resolution and main characteristics of BH model implemented in the simulations performed for this work, which are described in the next section.

4. Simulations

To assess the performance of the novel DF correction and to compare it with other prescriptions (Sect. 2.2), we carried out a set of two zoom-in simulations (a group-sized and a cluster-sized halo), and a cosmological box (with side length of 16 cMpc), all at the same resolution. This allowed us to test the new implementation in different environments. All simulations are performed assuming a ΛCDM cosmology with $\Omega_m = 0.24$, $\Omega_b = 0.0375$ for the total matter and baryon density parameters, $h = 0.72$ for the Hubble parameter, $n_s = 0.96$ for the primordial spectral index, $\sigma_8 = 0.8$ for the power spectrum normalization. We report in Table 2 a description of the main characteristics of these simulations. The selected zoom-in regions belong to the `Dianoga` simulation set introduced by Bonafede et al. (2011) and Bassini et al. (2020). We refer to such papers for a detailed description of this set of zoom-in initial conditions for simulations of galaxy clusters, as well as for details on the model of star formation and chemical enrichment adopted. The `D9` cluster has a mass $M_{200} \simeq 1.53 \times 10^{14}$ $M_\odot$ at $z = 0$, while the other refers to a lower-mass group of $M_{200} \simeq 1.38 \times 10^{13}$ $M_\odot$, namely `Cl13`[3].

[3] We indicate with M_{200} the total mass contained within a sphere of radius R_{200} which contains an overdensity equal to $200\rho_c(z)$, where $\rho_c(z) = 3H(z)^2/8\pi G$ is the critical cosmic density at redshift z. In Table 2 we use the *virial radius* $R_{\rm vir}$ defined as the radius within which the

Table 1: Summary of the relevant equations and parameters that characterize the sub-resolution model of BH evolution and AGN feedback. See Sect.3 for additional details. Column 1: values of the masses of the different particle species in the high-resolution regions of `Dianoga` clusters and `Cosmobox`: $m_{\rm DM}$, $m_{\rm gas}$ and m_*, are the masses of DM, gas and star particles, respectively; $\epsilon_{\rm DM}$, $\epsilon_{\rm gas}$, ϵ_*, and $\epsilon_{\rm BH}$ are the Plummer-equivalent softening lengths of the different particle species. For BH, gas and star particles, the softenings are fixed in comoving units. For DM particles, we fix the softening in comoving units until $z = 2$, and then in physical units until $z = 0$. Column 2: criteria for BH seeding: $M_{\rm BH,seed}$ is the seeding mass of a BH; M_0 is the minimum BH mass seed; $M_{\rm DM,h}$, $M_{\rm gas,h}$ and $M_{*,\rm h}$ are the halo masses in the DM, gaseous and stellar components; $M_{\rm h}$ is the total halo mass and $M_{\rm h,seed}$ is the minimum halo mass required to seed a BH. Column 3: BH mass accretion rate: $\dot{M}_{\rm Bondi}$ and $\dot{M}_{\rm Edd}$ are defined in Eqs.11, 12. Column 4: criteria for BH-BH merging: $\Delta r_{\rm BH}$ is the distance between the merging BHs, $d_{\rm merg}$ is the minimum threshold distance required for merging, $\Phi_{\rm BH_1}$ and $\Phi_{\rm BH_2}$ are the values of the gravitational potentials of the two BHs, $v_{\rm rel}$ the module of their relative velocity, $c_{\rm s}$ the local sound speed and a is the scale factor. Column 5: expression of the rate of the feedback energy released by the BH and thermally coupled to the surrounding gas; c is the light speed, $\eta_{\rm r}$ and $\eta_{\rm f}$ are the radiative and coupling efficiency, respectively.

Resolution	Seeding	Accretion	Merger	Feedback
Mass $m_{\rm DM} = 4.69 \times 10^7$ M$_\odot$ $m_{\rm gas} = 8.67 \times 10^6$ M$_\odot$ $m_* = 8.7 \times 10^6$ M$_\odot$ Force softening $\epsilon_{\rm DM} = 4.13$ ckpc / 1.38 kpc $\epsilon_{\rm gas} = 1.38$ ckpc $\epsilon_* = 0.35$ ckpc $\epsilon_{\rm BH} = 0.35$ ckpc	$M_{\rm BH,seed} = M_0 \frac{M_{*,\rm h}}{f_* M_{\rm DM,seed}}$ $M_0 = 2.7 \times 10^5$ M$_\odot$ $M_{\rm h,seed} = 6.94 \times 10^{10}$ M$_\odot$ $\frac{M_{*,\rm h}}{M_{\rm h}} = 2\%$ $\frac{M_{*,\rm h}}{M_{\rm DM,h}} = 5\%$ $\frac{M_{\rm gas,h}}{M_{*,h}} = 10\%$	$\min(\dot{M}_{\rm Bondi}, \dot{M}_{\rm Edd})$	Threshold distance: $\Delta r_{\rm BH} < d_{\rm merg}$ $d_{\rm merg} = 5 \cdot \epsilon_{\rm BH}$ Gravitationally bound: $\frac{\lvert\Phi_{\rm BH_1} - \Phi_{\rm BH_2}\rvert}{a} < 0.5 \cdot c_{\rm s}^2 - v_{\rm rel}^2$	$\dot{E}_{\rm feed} = \eta_{\rm r}\eta_{\rm f}\dot{M}_{\rm BH}c^2$ $\eta_{\rm r} = 0.1$ Quasar : $\eta_{\rm f} = 0.05$ Radio: $\eta_{\rm f} = 0.2$

Table 2: Set of the simulations. Column 1: simulation name; Column 2: method to account for unresolved DF; Column 3 and 4: virial mass and virial radius, respectively, at $z = 0$, of the most massive halo in the simulations.

Simulation	Name	$M_{\rm vir}$ [10^{13} M$_\odot$]	R$_{\rm vir}$ [kpc]
`Cl13`	`REPOS`	1.27	610.89
	`DYNMASS`	1.26	609.33
	`DYNFRIC`	1.26	609.75
`D9`	`REPOS`	18.76	1497.17
	`DYNMASS`	19.02	1504.28
	`DYNFRIC`	18.89	1499.24
`CosmoBox`	`REPOS`	2.57	751.01
	`DYNMASS`	2.58	751.55
	`DYNFRIC`	2.65	760.15

Both objects have been simulated at the same mass and spatial resolution (see Table 1).

As for the cosmological box, namely `CosmoBox`, it has been simulated by adopting exactly the same cosmological model and the same implementation of all physical processes as the zoom-in simulations. For each initial condition of `D9`, `Cl13`, and `CosmoBox`, we carried out three simulations using the same settings while changing only the sub-resolution technique to cope with the BH dynamics. We compared the repositioning scheme, the adoption of a boosted dynamical mass and the new implementation of DF introduced in Sect.2. In the following sections, we will refer to these schemes as, respectively, `REPOS`, `DYNMASS` and `DYNFRIC`. Comparing the results of these simulations allows us to assess the effect of our new implementation of DF with respect to some previously adopted ad-hoc prescriptions to account for this effect.

In the following sections, we will present our results using two different approaches. In Sect. 5, we will conduct a statistical analysis to show how the method to track BH orbits impacts on the properties of their population. Sect. 6 is dedicated to the study of the evolutionary dynamic histories of individual BHs, comparing their path when they sink into the potential well of the host sub-halos and during mergers when governed by different sub-resolution prescriptions.

5. Properties of the BH population

The minimum aim of our DF model is to avoid spurious numerical effects that other methods may produce, as discussed in Sect. 2. Thus, in this Section, we analyse the overall properties of the population of SMBHs in our simulation, focusing on the ability of our DF model to: place and hold the BH at the center of the host galaxies (Sect. 5.1), prevent BH particles from spuriously wandering outside the host galaxies (Sect. 5.2), reproduce the co-evolution of BHs and host galaxies (Sect. 5.4).

5.1. Centering the BHs within host galaxies

To assess the ability of each model to correctly locate the BHs at the centre of the host sub-halos, we select all the main halos and sub-halos having a BH within their DM half-mass radius (hereafter R$_{\rm HMS}$). Sub-halos are identified by the `SubFind` algorithm (Springel et al. 2001b; Dolag et al. 2009) and are requested to

mean halo density corresponds to the prediction of spherical collapse (e.g. Eke et al. 1996). Accordingly, the *virial mass* M$_{\rm vir}$ is the mass of a sphere enclosed within a radius R$_{\rm vir}$.

feature at least 20 particles. In the zoom-in simulations, we excluded from the analysis all the halos that contain within their R_{200} at least one low-resolution DM particle spuriously scattered within the high-resolution region. We then calculated the distance between the (sub-)halo centers and the closest BH. Figure 1 shows the histogram of the probability density function (PDF) of the number of (sub-)halos having a BH within their R_{HMS}, versus the distance Δr from the associated BH. The sample of sub-halos in Fig. 1 is obtained by summing up all the (sub-)halos from D9, Cl13 and CosmoBox. In each column, we compare different prescriptions for BH dynamics with the DF model, shown in blue, and we report the results at $z = 3$, 1 and 0, from top to bottom. For reference, the dashed-dot vertical line marks the value of the Plummer-equivalent softening length of BH particles. Not surprisingly, the REPOS prescription predicts sub-halos that host generally well-centered BHs. This is the most consistent advantage of the repositioning technique, as well as the most predictable, since it explicitly forces the BHs to be relocated at each time-step at the center of their host substructures. As for the DYNMASS, it shows the less pronounced tail for higher distances ($\Delta r > 1$ ckpc) at $z = 3$. In fact, at high redshift, the impact of a large dynamical mass is relatively more important given that a larger number of BHs is expected to have relatively smaller true mass and live in less resolved hosting halos. Interestingly, in this regime, our DF model performs quite well in keeping BHs at the center of their host halos, without resorting to ad-hoc prescription. The comparable performance of the two methods is actually a non-trivial and encouraging result for our DF implementation; in fact, accurate centering of the BHs in sub-halos is obtained as a result of an implementation of the DF correction instead of an artificial increase of BH masses, which have the side effect of altering the structure of the sub-halos gravitational potential, thereby impacting on the resulting galaxy formation process (e.g. Chen et al. 2022). Table 3 reports the percentage of sub-halos with which each simulation contributes to the differential distribution of Fig.1. The D9 simulation provides the most numerous population of centered sub-halos, with at least 70% of the total distribution.

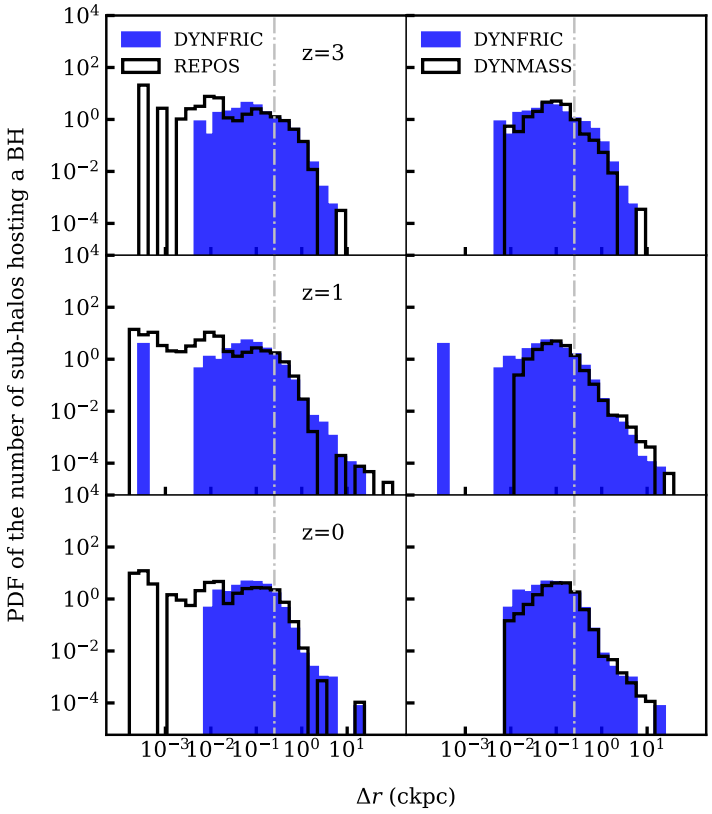

Fig. 1: Probability density distribution of the distances between sub-halos identified by SubFind and the closest BH particle within the R_{HMS} of each sub-halo of Cl13, D9 regions and Cosmobox. The rows show the results obtained at different redshifts: $z = 3$ (up), $z = 1$ (central) and $z = 0$ (bottom). The column report the results comparing DYNFRIC and REPOS on the left, and DYNFRIC and DYNMASS on the right side. We include a dashed-dot line in each plot indicating the softening length of the BH as a reference for the spatial resolution of the simulation.

5.2. The population of wandering BHs

Another crucial aspect to consider when judging the reliability of a DF model is its capability of preventing BHs from escaping the host sub-halos because of two-body interactions with larger-mass particles or during merger events. We denote the population of these kicked-off BHs as *wandering* BHs. We classify a BH as wandering whenever its distance from the closest sub-halo is larger than twice the R_{HMS} of the closest sub-halo.

Figure 2 shows the cumulative fraction of wandering BHs to the total number of BHs as a function of BH mass at $z = 0$ in the left panel and as a function of redshift in the right panel, for all the considered sub-resolution models. In the left panel, for each BH mass on the x-axis we see the cumulative fraction of wandering BHs on the y-axis. We observe that, irrespective of the method employed to keep the BH centered, the ratio of the wandering BHs to the total number of BHs increases as we progressively consider larger BH masses at the numerator. Each curve extends up to the value of the mass of the most massive wandering BH found in the considered simulation. The REPOS simulation, in particular, exhibits the higher fraction of wandering BHs. The percentage of wandering BHs in the simulation using the repositioning scheme rises for massive BHs ($M_{BH} > 10^7 M_\odot$). This is somewhat surprising since massive BHs are those for which DF should be better numerically resolved and, therefore,

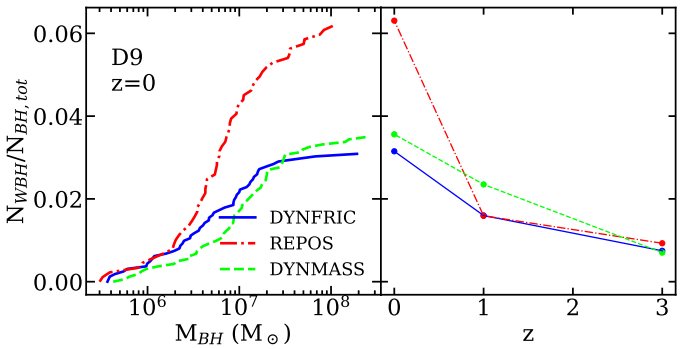

Fig. 2: Cumulative number of wandering BHs to the total number of BHs found in the D9 region, as a function of the BH mass at $z = 0$, in the left panel, and as a function of redshift for $z = 3$, $z = 1$, $z = 0$ in the right panel. In the left panel, no mass threshold is adopted to select the BHs, hence all the BHs with mass above the seeding mass are included (see Table 1). In both panels, the simulation using the DF model, marked with a blue line, is compared with REPOS in red and DYNMASS in green. The wandering BHs are defined as those having a distance larger than two times the R_{HMS} from the closest sub-halo.

Table 3: Percentages of sub-halos from each simulation that contribute to the distributions shown in Fig.1. For each implementation, we indicate the percentage of sub-halos for each simulation: Cl13, D9 and Cosmobox, in the left, central and right columns, respectively. Percentages are listed for different redshifts (as in Fig.1): $z = 3$, $z = 1$, and $z = 0$.

	REPOS			DYNMASS			DYNFRIC		
	Cl13	D9	CosmoBox	Cl13	D9	CosmoBox	Cl13	D9	CosmoBox
$z = 3$	11	82	7	12	83	5	12	83	5
$z = 1$	10	78	12	9	80	11	10	78	12
$z = 0$	13	70	17	10	75	15	10	75	15

less prone to wander outside their host galaxy. Moreover, the repositioning mechanism predicts the highest percentage of wandering BHs, substantially increasing from $z = 1$ to $z = 0$. The origin for the excess of wandering BHs in the REPOS scheme can be ascribed both to close encounters between sub-structures and, at decreasing redshift, to the presence of large-scale potential gradients. To illustrate how these mechanisms work, we show several wandering BHs in the two panels of Fig. 3.

Each panel of this figure shows, on the central plot, the projected stellar density around two wandering BHs, BH 2 in the top panel, and BH 4 in the bottom panel. We also show the position of the other BHs in the field, marking wandering BHs with cyan crosses and the BHs centered on their host as green crosses. Furthermore, the centers of neighboring sub-halos are denoted by shaded white dots, with circles corresponding to the sub-halo R_{HMS} enclosing them. The side plots display the gravitational potential Φ of the stars along the x-axis (on the top) and y-axis (on the right). In the top panel of Fig.3, BH 2 wanders due to a close encounter between two sub-halos, one having a deeper potential well. BH 2 then migrates to the location of the most bound neighbour particles, thus moving along the gradient of the potential of the central sub-halo, and leaving its initial host sub-halo. It is worth noticing that, as defined here, a BH lying within twice the R_{HMS} of a sub-halo can be a wander: our definition classifies as not wandering only those BHs located within twice the R_{HMS} of the closest sub-halo. The bottom panel of Fig. 3 shows the position at $z = 0.06$ of the supermassive wandering BH 4 with a mass of 10^{10} $M_\odot$. Being embedded in the large scale potential gradient of the most massive halo, depicted in the side plots of the panel, BH 4 escaped from its original sub-halo. This demonstrates that for the repositioning scheme implemented in this work, even the most massive BHs can move away from their host galaxies, thereby completely changing their gas accretion and the ensuing release of feedback energy.

In the simulations using the DF correction and DYNMASS, wandering BHs instead originate from two-body or even three-body scattering. When the BH is not repositioned, the dynamics during these events can be quite complex, and will be analyzed in more detail in Sect. 6.

Finally, Fig. 4 displays the position of all the BHs in a projected stellar density map within 1 Mpc from the center of the most massive halo in the D9 simulation at redshift $z = 0$ for REPOS (top panel), DYNMASS (bottom left panel) and DYNFRIC (bottom right panel). We plot BHs with crosses of different colors depending on their distance Δr from the closest sub-halo, comparing it to the R_{HMS} of this sub-halo. Dark-blue crosses indicate BHs with $\Delta r < R_{HMS}$, green crosses are for $R_{HMS} \leq \Delta r < 2 \times R_{HMS}$, and cyan crosses mark the wandering BHs, i.e. those with $\Delta r \geq 2 \times R_{HMS}$. We also plot the circles the ten most massive sub-halos in the region, each having radius that is suitably scaled according to the value of its R_{HMS}. Each circle is centered on the sub-halo position and has a radius proportional to its R_{HMS}. The radius of the yellow circle corresponds to the actual physical value of the R_{HMS} of the BCG. For the purpose of readability, we adopted a different scaling for marking the size of the other sub-halos, as indicated in the figure legend.

Figure 4 shows that the DYNFRIC simulation exhibits the less numerous population of wandering BHs, mainly located close to multiple BH systems. Most of the DYNMASS wandering BHs occupy the central region of the halo. However, crucial differences arise between REPOS and the outcomes of the other simulations: the overall population of BHs using the repositioning scheme, significantly decreases both in the core and in the outskirt of the halo. Most of the sub-halos, identified by stellar density peaks or with circles for the more massive ones, lacks a central BH.

5.3. Merger events and multiple BH systems

The occurrence and timing of merger events are highly sensitive to the prescription to control the BH dynamics. We observe that the REPOS simulations facilitate mergers when two BHs approach a distance $d_{\rm merg}$ (see Table 1), making them merge on shorter timescales than when the other prescriptions are adopted (see Sect. 6).

Fig. 5 displays the cumulative (upper part) and the differential (lower part) distributions of the number of merger events as a function of the redshift, for the three simulations. DYNFRIC and DYNMASS simulations predict similar results, with DYNFRIC showing slightly more mergers in denser regions (Cl13 and D9) and less mergers in the CosmoBox simulation. By contrast, all the simulations based on REPOS feature a significantly higher number of mergers, more than twice the number of mergers of both DYNFRIC and DYNMASS in the zoom-in simulations and more than three times in the CosmoBox simulation. Interestingly, the density peak of mergers for the repositioning model occurs at $z \simeq 1.5$ in all the simulations.

Before the merging events occur, one would expect to find structures hosting systems of two or more BHs. However, the increase of mergers in the repositioning scheme is not counterbalanced by an increase of multiple systems, i.e. of structures containing two or more BHs. Fig. 6 shows the ratio between the number of sub-halos hosting more than one BH within the R_{HMS} to total number of sub-halos hosting at least one BH for $z = 3, 1, 0$ in the D9 simulations. While the percentage of sub-halos hosting multiple BHs reaches more than the 8% in DYNFRIC (blue) and DYNMASS (green) simulation, the REPOS shows a consistently lower percentage. The concurrence of a larger number of mergers and the nearly absence of multiple systems found for the REPOS simulations can be ascribed to extremely fast mergers, with multiple BHs coexisting within the same halo only for a rather short time.

We note that the number of merger events is influenced both by the adopted model to trace the BH dynamics and by the specific seeding prescription adopted. In principle, a higher number

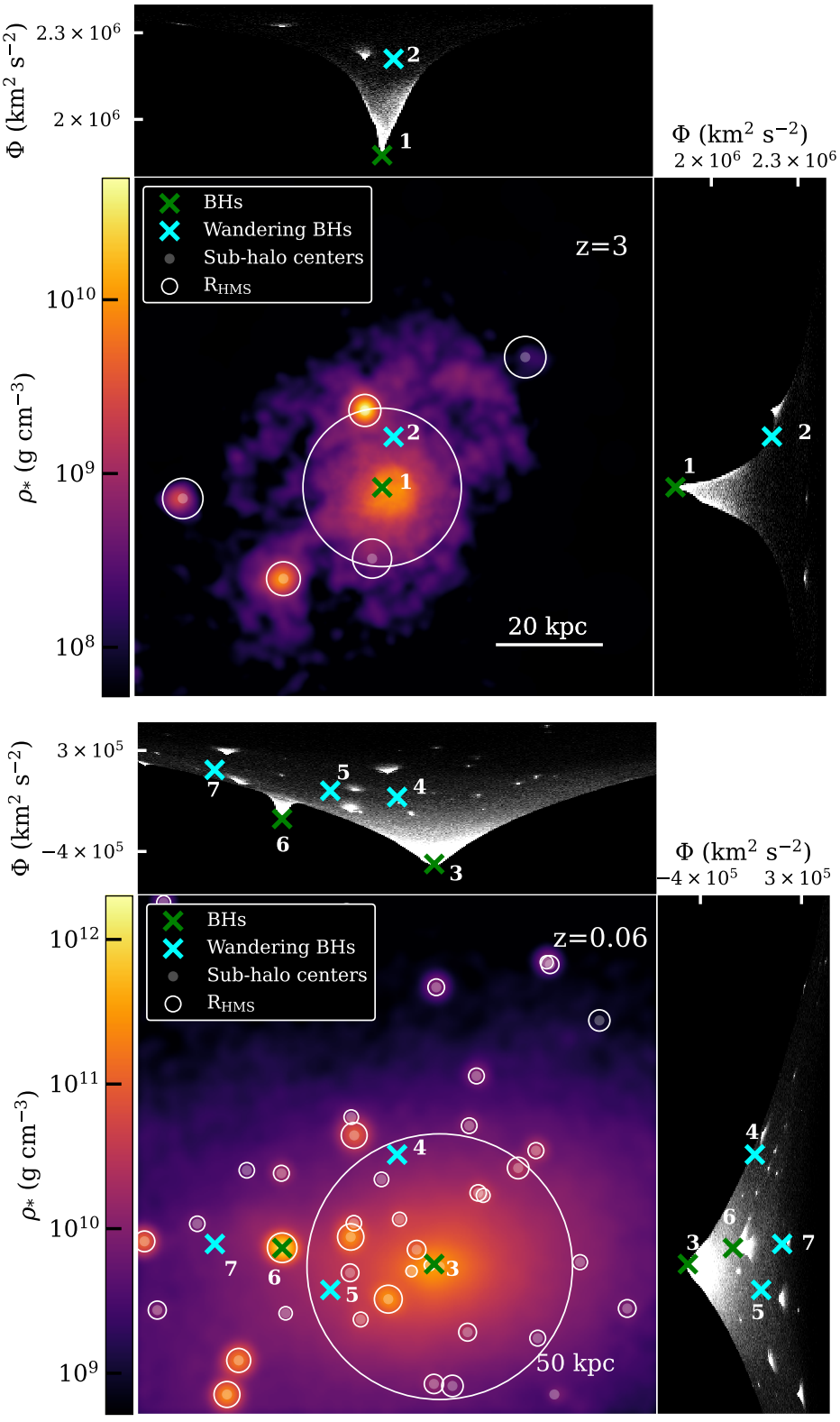

Fig. 3: Stellar density projection along the z-axis with depth of 100 kpc (top) and 300 kpc (bottom), centered on the position of a wandering BH at redshift $z = 3$ (tagged as BH 2; left panel), and of a wandering BH at $z = 0.06$ (tagged as BH 4; right panel) in the D9 simulation using the REPOS scheme. In both panels, the cyan crosses identify the wandering BHs, while the green crosses identify the BHs centered in their host. We show sub-halo centers as white shaded dots, with the white circles indicating the corresponding R_{HMS}. On the top and on the right of each panel we show the gravitational potential Φ of all the star particles (light white dots) and of the BHs (crosses) in the field, projected along the two orthogonal directions.

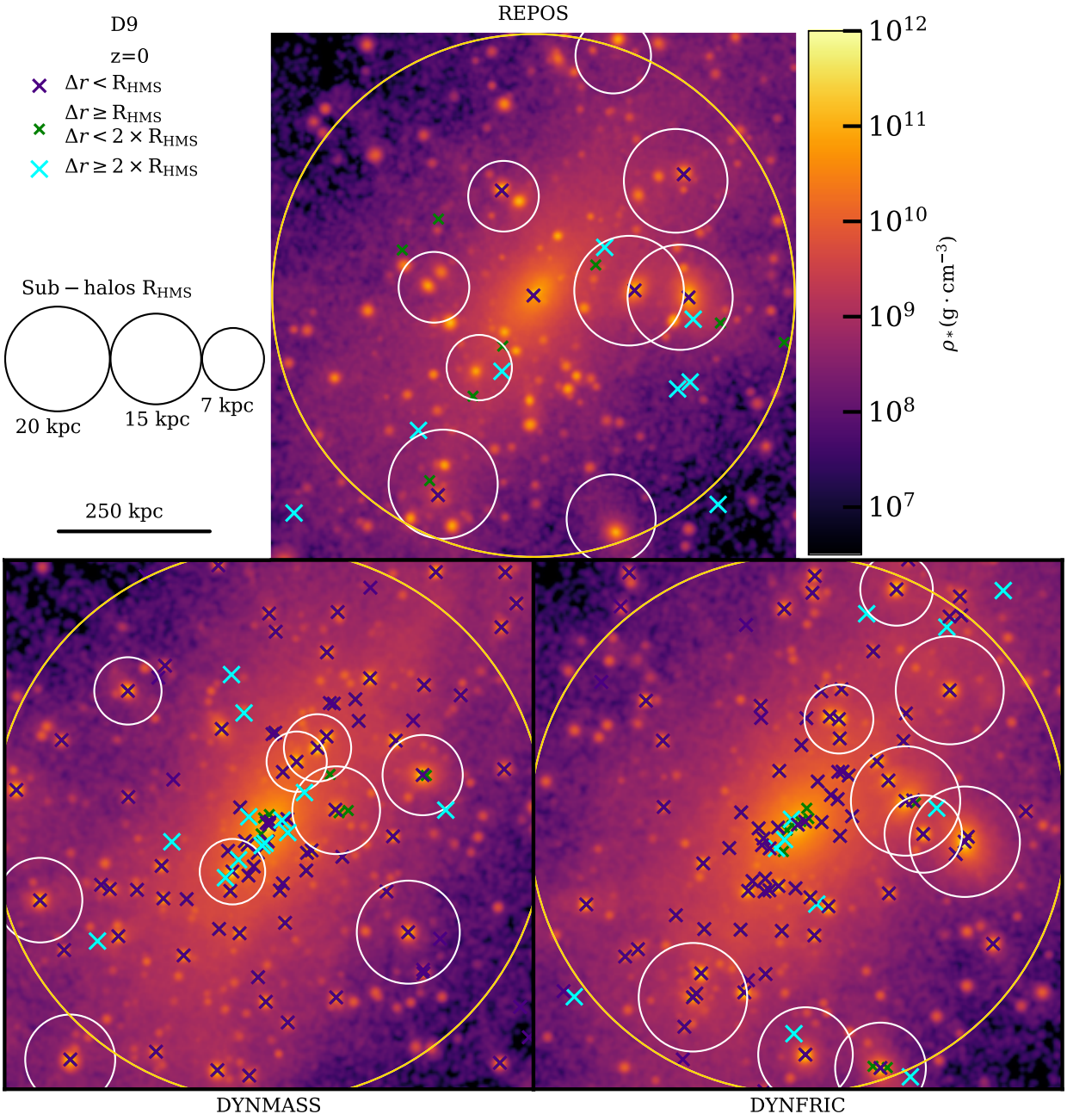

Fig. 4: Stellar density maps along the z-axis with depth of 1 Mpc centered on the most massive halo of D9 at $z = 0$ in the REPOS (top), DYNMASS (bottom left) and DYNFRIC (bottom right) simulations. The panels are all 1 Mpc on a side. In each panel, we plot with dark-blue crosses the BHs located within the R_{HMS} of the associated sub-halo (the same criterion adopted in Sect. 5.1). BHs lying between R_{HMS} and 2 rmR_{HMS} of the closest sub-halo are indicated with green crosses, while wandering BHs (defined as those located beyond $2R_{HMS}$ of the closest sub-halo) are shown as light-blue crosses. The values of R_{HMS} of the ten most massive structures correspond to the radii of the circles, each centered on the position of the corresponding sub-halo. The R_{HMS} of the BCG, in yellow, corresponds to the physical size of the yellow circle. The legend in the upper left panel of the plot shows the scaling size of the other sub-structures in the region, marked in white.

of merging events may be associated with a more frequent seeding. This situation may arise when, following a merging event between BHs but not between their corresponding halos, one of the two halos remains orphan of its BH, while still matching the seeding conditions (see Table 1). In this case, a new BH would be seeded at the center of the orphan halo, thereby possibly contributing to increase the BH-BH merger rate. To quantify how this "seeding bias" affects the merging predictions of from each model, we report in Table 4 the number of seeded BHs in each simulation.

We observe that the increase in the total number of seeded BHs in the REPOS simulations is only marginal. The absence of a proportional rise in the number of seeding black holes despite the increase in mergers in the REPOS simulations can be addressed on the concurrence of two particular seeding conditions.

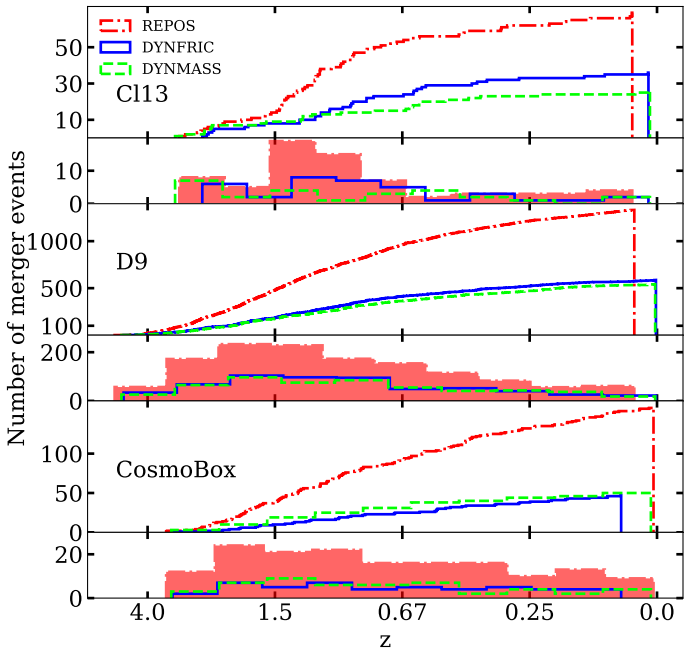

Fig. 5: Cumulative and differential distributions of the number of merger events as a function of redshift. Cl13, D9 and CosmoBox are on the first, second and third row, respectively. The REPOS simulation results are marked with a dash-dotted red line (with a shaded area marking the differential distributions), the DYNFRIC simulations with a blue solid line and the DYNMASS simulations with a dashed green line. The curves stop at the redshift corresponding to the occurrence of last merger event.

Table 4: Number of seeded BHs in each simulation for every sub-resolution prescription adopted.

Simulation	REPOS	DYNFRIC	DYNMASS
Cl13	206	191	184
D9	2239	2206	2169
CosmoBox	328	314	323

On the one hand, the seeding occurs exclusively within the main halos identified by the FoF halo finder, and not within the sub-halos identified by SubFind. On the other hand, BHs are not seeded in FoF groups which already contain a BH particle. Instead, the more frequent scenario in the REPOS simulations is the merging of two BHs initially belonging to two sub-structures contained within the same FoF halo. In this case, no further seeding takes place within the sub-halo which eventually remain orphan of its BH.

5.4. The M_*–$M_{\rm BH}$ relation

A first diagnostic to investigate how the processes of star formation and galaxy evolution are intertwined with the evolution of the population of SMBHs is to look at the relationship between SMBH masses and stellar masses of the bulges of the host galaxies, the so-called Kormendy-Magorrian relation (Kormendy et al. 1993; Magorrian et al. 1998). Figure 7 shows this relation obtained by varying the implementation for the BH dynamics in all the simulations for the three initial conditions considered in our analysis. In detail, for each halo with a mass larger

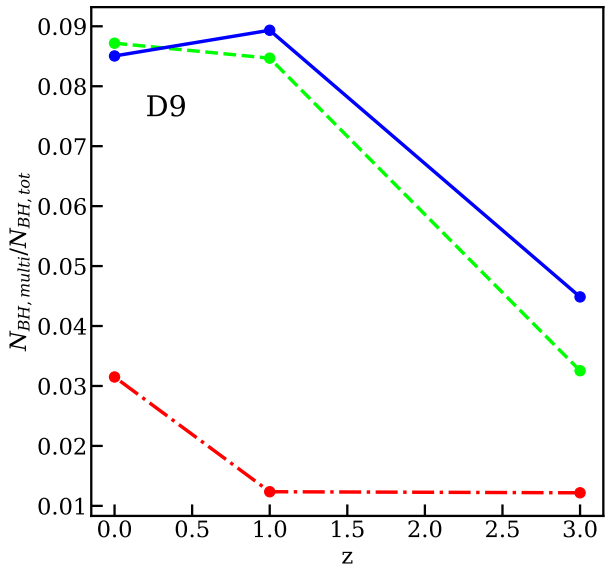

Fig. 6: The ratio between the number of sub-halos hosting more than one BH to the total number of sub-halos hosting at least one BH in D9 simulations. We consider DYNMASS (dashed green line), DYNFRIC (solid blue line) and REPOS (dot-dashed red line) at $z = 3, 1, 0$.

than a threshold value $M_{\rm thr} = 10^{10} M_\odot$, we distinguish between the central galaxy, to be identified with BCG or Brightest Group Galaxy (BGG; marked with diamond symbols in Fig. 7), and the satellite galaxies, which are hosted within the substructures identified by SubFind (marked with circles). For the BCGs, we calculate the stellar mass of the stars belonging to the BCG/BGG. within 70 kpc from the center, to avoid contributions from the intra-cluster light. As for the satellite galaxies, their stellar mass is computed by considering all the star particles that SubFind assigns to the substructure. For the central galaxies, we associate the most massive BH within 70 kpc from the center of the structure. For the satellite galaxies, we link the closest BH within their $R_{\rm HMS}$. Symbols are color-coded according to the distance between the galaxy centers and the associated BHs. For reference, in each panel we also show the relation obtained by McConnell & Ma (2013) and the data for BCGs and BGGs as measured by Gaspari et al. (2019). We note in general that all the simulations reproduce rather well the observational relation, possibly with a slightly larger normalization. Besides proving the good calibration of the AGN feedback parameters, this agreement also demonstrates that this scaling relation is relatively insensitive to the details of the model adopted to account for unresolved DF on BH dynamics.

Table 5 presents data on stellar mass, associated BH mass, and the distance of the BH from the halo center for the most massive halo within each simulation. The DYNFRIC simulations predict better centered BHs compared to the DYNMASS simulations.

As for Cl13, we note that the DYNFRIC, REPOS and DYNMASS simulations all produce very similar results. In all the three cases, the stellar mass of the BGG, and the mass of the hosted SMBHs are quite similar at $z = 0$.

In the D9 region, the larger statistics of sub-halos helps to better understand what happens in different scenarios. Still, the DYNFRIC and the DYNMASS simulations produce comparable results, with the DYNFRIC simulation even further reducing the off-

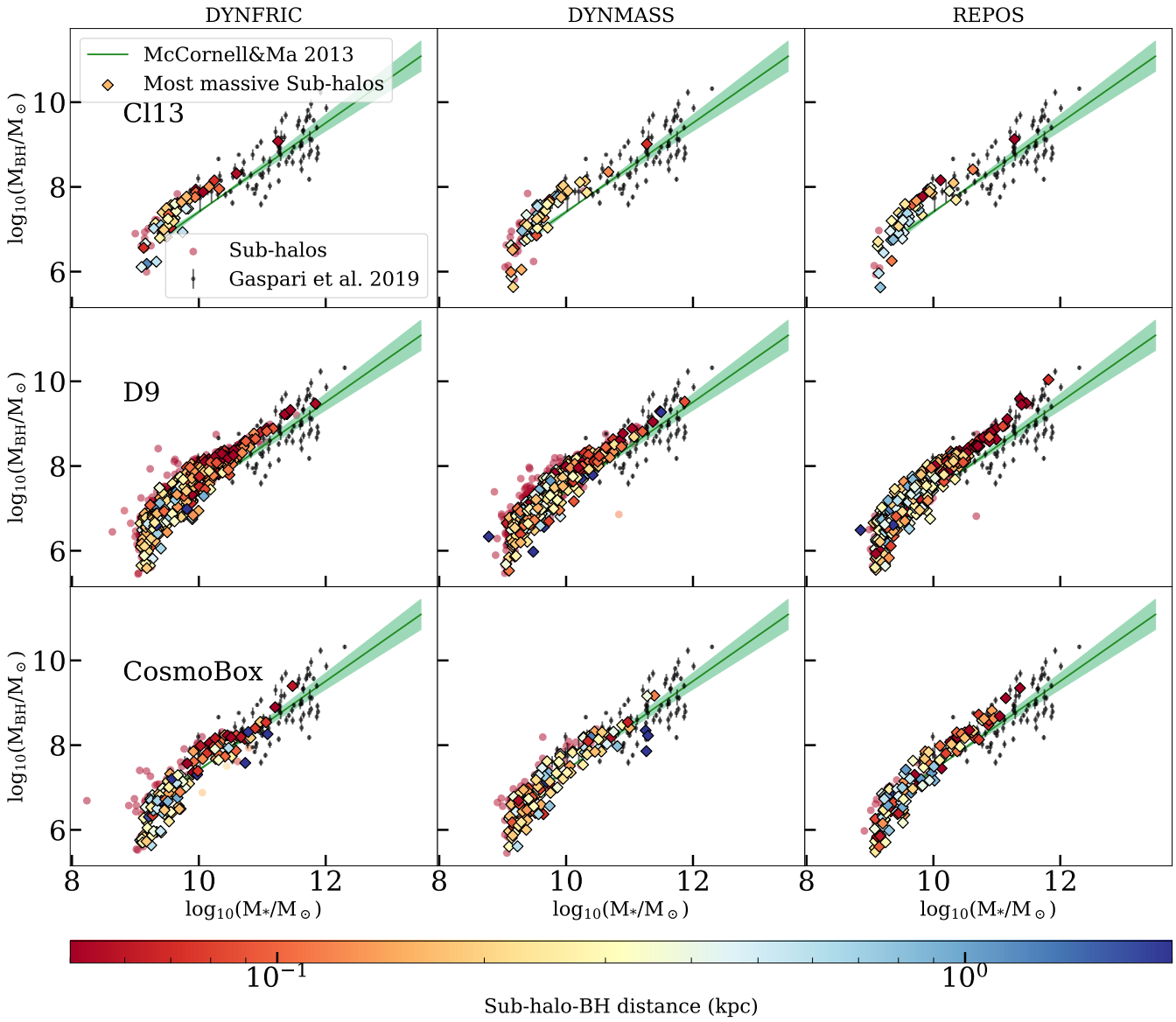

Fig. 7: The relationship between BH mass and stellar mass of the host galaxies for `Cl13` (upper panels), `D9` (central panels) and `CBox` simulations (lower panels). Each column contains the results obtained with a different BH dynamics prescription: `DYNFRIC` (left), `DYNMASS` (central), `REPOS` (right). The diamonds refer to the BHs associated to the main halos while circles correspond to sub-halos belonging to halos more massive than 10^{10} $M_\odot$. Diamonds and circles are color-coded according to the distance between the sub-halo centers and the associated BHs. For comparison, we also plot observational data from Gaspari et al. (2019) with black dots with errorbars, and the relation obtained by McConnell & Ma (2013) with a green and shaded area.

set of the most massive BHs from the center of their host galaxies. The results for the `D9` region using `REPOS` are in good agreement with the observational data for $M_* < 10^{11}$ $M_\odot$. However, this simulation predicts BHs that are more massive compared to the other implementations, again due to excess of merging episodes, as already discussed. We note that the BH having the highest mass in the `D9` region results from the merging between the BH 3 and the massive wandering BH 4 in Fig. 3 that reached the center of the BCG from $z = 0.06$ to $z = 0$.

Finally, the `CosmoBox` results confirm the substantial agreement between our predictions and observations. The DF model further demonstrates its increased efficiency in centering the BHs compared to `DYNMASS`. Nonetheless, both simulations reveal three massive sub-halos with a stellar mass $> 10^{10.5}$ $M_\odot$, whose BHs have a significant displacement. The visual representation of these three occurrences is depicted in Fig. 8, which shows the projection of the stellar density centered around these pathological sub-halos. In the first row, two analogous situations are presented: a close encounter between two substructures hosting BHs of different masses. The displacement obtained in Fig. 7 follows from the association of the most massive BH to the central halo, marked in Fig.8 with a red circle. This feature, rather than being a real off-centering of the BH, is a consequence of the method that we adopted to associate a BH to a given structure.

The third sub-halo, shown in the bottom right panel of Fig.8, hosts a truly off-center BH. This is the outcome of a merger event between two substructures which took place at redshift $z = 0.19$ (see bottom left panel). Since then, the BH belonging to the merging substructure did not have the time to sink to the

Table 5: Stellar mass (left column), associated BH mass (central column) and its distance from the halo centers (right column) for the most massive halo identified within each simulation.

	$\log_{10}(M_*/M_\odot)$	$\log_{10}(M_{BH}/M_\odot)$	Distance (kpc)
C113			
REPOS	11.28	9.13	0.03
DYNMASS	11.27	9.01	0.10
DYNFRIC	11.25	9.07	0.07
D9			
REPOS	11.75	10.0	0.10
DYNMASS	11.89	9.52	0.12
DYNFRIC	11.83	9.47	0.07
CosmoBox			
REPOS	11.36	9.35	1.25×10^{-3}
DYNMASS	11.39	9.16	0.16
DYNFRIC	11.47	9.4	0.08

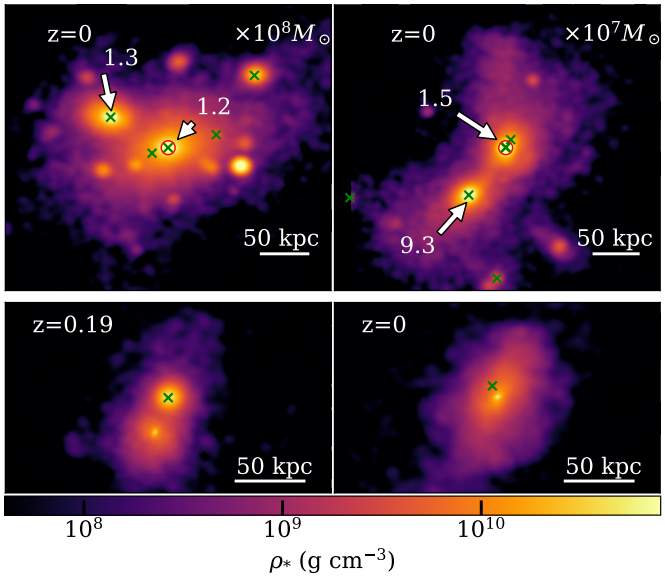

Fig. 8: Stellar density maps along the z-axis with depth of 350 kpc (upper row) and 260 kpc (bottom row) of the massive sub-halos having a large separation between sub-halo center and the associated BH in the CosmoBox simulation, using the DYNFRIC model (blue diamonds in the corresponding plot in Fig.7, for $\log_{10}(M_*/M_\odot) > 10$), at redshift $z = 0$. BHs are marked by green crosses. Upper panels: two close encounters between structures. The halo center is identified as a red circle. The arrows link to the values of the BH masses (in units as specified in the label). In both the left and right panels, the most massive BH belongs to the off-center substructure. Bottom panels: a merger event between two substructures at redshift $z = 0.19$ (left panel) and the resulting merged halo at $z = 0$ (right panel). The plot on the right side captures an off-center BH while sinking toward the halo center.

center of the merged sub-halos, hence the displacement at $z = 0$ between the center identified by SubFind and the BH.

Table 6: Column 1 and 2: initial true masses of the central ($m_{BH,cen}$) and satellite ($m_{BH,sat}$) BHs in the events described in Sect.6, at the initial redshifts $z = 3$ (for Events 1 and 2) and $z = 1.26$ (for Event 3). In the Events 1 and 2, the BH masses of both BH_{cen} and BH_{sat} are boosted in the DYNMASS runs. On the other hand, we only boost the satellite BH mass in the Event 3. Column 3: mass of the sub-halo hosting the events. Column 4: initial distance between the two BHs.

	$m_{BH,cen}$ ($M_\odot$)	$m_{BH,sat}$ ($M_\odot$)	M_{sub} ($M_\odot$)	Δr (kpc)
Event 1	3.23×10^5	3.63×10^5	6.96×10^{10}	4.08
Event 2	3.60×10^6	7.20×10^5	8.11×10^{10}	1.48
Event 3	6.39×10^8	2.04×10^6	4.50×10^{11}	10

6. Analysis of individual events

Besides the analysis of the properties that emerge from the population of BHs in each simulation, we perform a detailed study of the effect of different sub-resolution prescriptions on the dynamics of single BHs.

To better understand the BH dynamics, due to the different prescriptions to follow it, we adopt the following approach. We freeze the configuration of BHs and of their host galaxies at two snapshots from the C113-DYNMASS simulation at $z = 3$, and $z = 1.26$. Using these snapshots as initial conditions, we run simulations using: the DYNFRIC model introduced in Sect.2.1, the DYNMASS method based on boosting dynamical mass at seeding (see Sect. 2.2.2), the REPOS method based on relocating the BH on the local potential minimum (see 2.2.1), and a fourth simulation not correcting to the BH position is introduced (NOCORR in the following). The simulations having as initial conditions the snapshot at $z = 3$ evolve until $z = 2$, while the ones starting at $z = 1.3$ reach $z = 0.95$. In this way, we trace the histories of BHs that, at the beginning of the simulations have the same position, mass and velocity, and are located in substructures with the same characteristics. Therefore, any difference between their subsequent orbits is purely driven by the different tracing methods adopted. To ensure that the results were reproducible and marginally affected by the possible chaotic nature of a simulation, we carried out each of them twice, obtaining results which show marginal differences in the timings, while leaving the general results qualitatively unchanged. In particular, our analysis focuses on the evolution of binary BH systems, typically characterized by a massive BH located at the centre of a substructure, indicated as BH_{cen}, and a second displaced BH, the "satellite", labelled as BH_{sat}. We focus in the following on three events which represent three very different values of the central-to-satellite mass ratio between the BHs, $f_m = m_{BH,cen}/m_{BH,sat}$; they are labelled as Event 1, Event 2 and Event 3 in the following. Event 1 consists of a binary system of two BHs initially displaced by 4 kpc from each other. The initial BH mass ratio is $f_m = 1.1$, and both the BHs have a mass smaller than m_{DM} (see Table 6). For that reason, both masses are boosted in the DYNMASS simulation. Event 2 involves a binary system of two BHs, initially at a distance of 1.5 kpc, with a higher mass ratio ($f_m = 50$) compared to Event 1, but at the same redshift. Still, the two masses are both increased in the DYNMASS run. Event 3 consists of a binary system of two BHs initially separated by 10 kpc at z = 1.26. The BHs have a large mass ratio $f_m = 313$. This time, only BH_{sat}, whose mass is less than m_{DM}, undergoes the dynamical mass correction in the DYNMASS simulation.

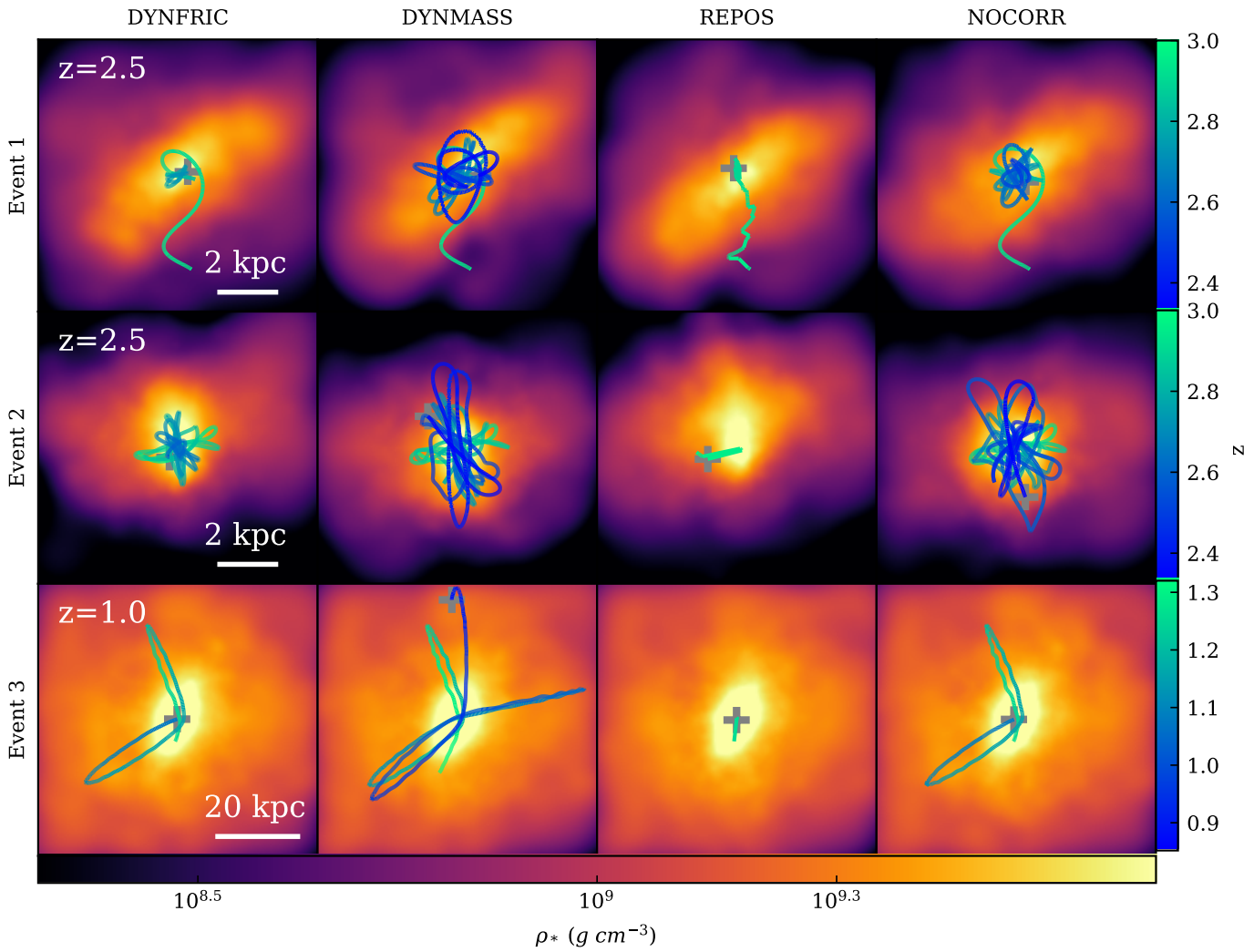

Fig. 9: Stellar density map along the z-axis with depth of 10 kpc in the top and central row and 70 kpc in the bottom row, centered on the central BH (BH_{cen}) of Event 1 in the top row, Event 2 in the central row and Event 3 in the bottom row. The maps refer to the final redshift at which each event is followed. In each panel, the line is the path of the satellite BH (BH_{sat}) involved in the merger event, color-coded according to the redshift. The crosses indicate the last position of the satellite BH before either the merging event or the end of the simulations (see Sect. 6). The columns display the BH evolution using different sub-resolution prescriptions, from the left: using DF (first column), using a boosted dynamical mass (second), adopting the repositioning scheme (third) and finally without any correction for BH dynamics (fourth).

The characteristics of these three events are summarized in Table 6. Figure 4 provides a graphical representation of the stellar density map at the redshift marking the conclusion of the simulation or the BH merger, whichever occurs first. The figure also includes the trajectory of the BH_{sat}, color-coded according to redshift, within the substructure hosting that event. Each row displays a single event, and results from the `DYNFRIC`, `DYNMASS`, `REPOS` and `NOCORR` simulations are presented from left to right in each column.

Figure 10 displays on the left column, for the different events in each row, the distance between BH_{cen} and BH_{sat}, namely Δr, during the event. The dashed green line, the solid blue line, the dash-dotted red line and the short-dashed orange line indicate the `DYNMASS`, `DYNFRIC`, `REPOS` and `NOCORR` runs, respectively. The horizontal grey solid line represents the distance threshold which is necessary for the merger event d_{merg} to happen (see Table 1). The right side of Fig.10 focuses on the results of the `DYNFRIC` runs. In particular, we plot Δr in the top panel, and the ratio between the DF force and the gravitational force (including the contribution of the DF correction), both for BH_{cen} (light-blue) and BH_{sat} (light green) in the bottom panel. In the following subsections, we will study each event separately.

6.1. Event 1

Looking at the upper row of Fig. 10, the simulation adopting the `DYNFRIC` model exhibits oscillations with gradually decreasing amplitude and gently drives the two BHs toward the merger. In the `DYNMASS` simulation, instead, the distance between the BHs exhibits persistent oscillations, which do not decrease in amplitude. Rather than driving the BHs to form a close pair, the enhanced dynamical mass intensifies their mutual gravitational attraction, causing collisions resulting in sustained relative distance fluctuations. The simulation that does not employ any cor-

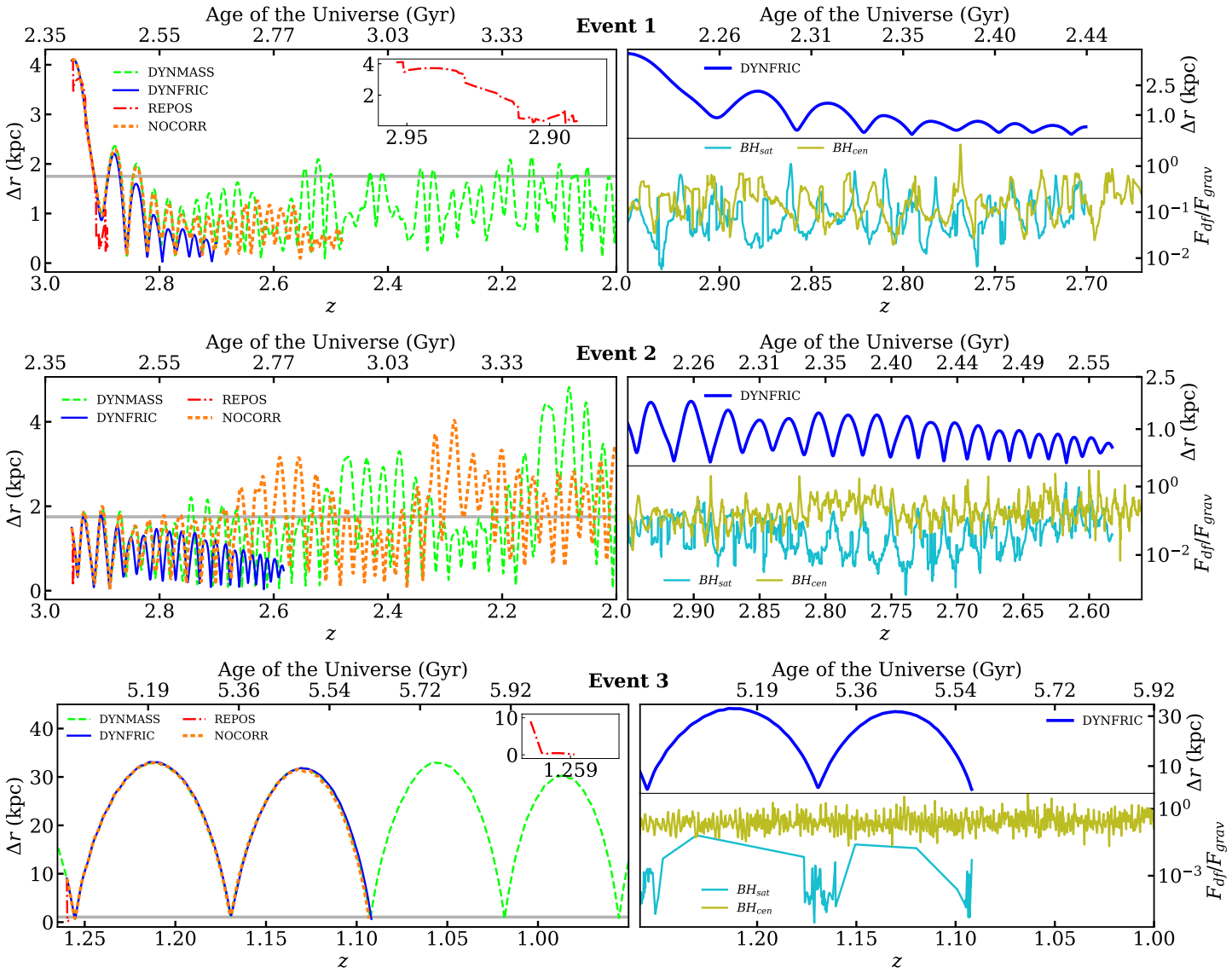

Fig. 10: Left column: evolution of the distance between the central and the satellite BH in Event 1 (top), Event 2 (central), Event 3 (bottom). The dashed green line displays the evolution using the dynamical mass scheme (DYNMASS), the blue solid line is for the DF scheme (DYNFRIC), the dash-dotted red line for the repositioning (REPOS), and the densely dashed orange line is for the case without any sub-resolution prescription (NOCORR). The horizontal grey solid line represents the distance threshold which is necessary for the merger event $d_{\rm merg}$ to happen. Right column: evolution of the distance between the BHs for the DYNFRIC case (top panel) and ratio between the DF and gravitational forces during each event.

rection shows, after an initial gradual decrease of the distance, a second phase during which the two BHs keep oscillating with respect to each other, with a nearly constant amplitude. The merger between the two BHs, which occurs right after $z \sim 2.5$, is preceded by a sudden decrease in distance. The inset in the upper right side zooms on the results of the REPOS simulation. We observe a merger event occurring very rapidly, with the distance between the two BHs decreasing through discrete "jumps" as large as almost 1 kpc.

The figure shows that the two BHs can be closer than $d_{\rm merg}$, yet without merging. We remind that, this represents a necessary, but not sufficient condition for the merger to happen. Indeed, merging requires the BHs to fulfill all the conditions listed in Table 1. Whenever they are closer than $d_{\rm merg}$, they merge if the gravitational binding criterion is also satisfied. From the visual representation of Fig.9 we can infer that DYNFRIC, DYNMASS and NOCORR show similar paths for $\rm BH_{sat}$ until it first crosses the denser region of the sub-halo. Then, DYNFRIC and NOCORR simulations bound $\rm BH_{sat}$ in the core of the host. Besides, DYNMASS reproduces constant oscillation at rather fixed apocentric distances. On the other hand, the path of $\rm BH_{sat}$ in the REPOS simulation is discontinuous and short compared to the other: through successive repositioning steps, the BH drops at the center of the sub-halo. The right panel of the plot highlights the features arising from the application of the DF correction in the DYNFRIC model. In this case, the DF force responds to a local increase of stellar density. The ratio between the gravitational and the DF forces oscillates for both BHs with oscillation of comparable amplitude, indicating that they are orbiting around a central denser zone. Indeed, looking at the upper row of Fig. 9 we observe that the final merger will take place in the central, denser region on the substructure.

6.2. Event 2

The second rows of Fig. 9 and of Fig.10 show the evolution of the distances during the Event 2. Again, throughout the event, REPOS and DYNFRIC lead to immediate and gradual BH coalescences of the BHs, respectively. DYNMASS and NOCORR do not produce any merger, thus leaving BH_{sat} swing around the central one. Thus, neither an ad-hoc increase of the BH mass nor the N-body gravity solver without any correction is sufficient to dump the oscillations of the smaller BH. Furthermore, the visual representation in Fig.9 demonstrate that DYNFRIC, DYNMASS and NOCORR simulations all produce an initial tilt of the orbit of BH_{sat} in the direction of the elongated denser region of the sub-halo. Then, in the DYNFRIC simulation, the contribution of DF leads the BH toward the center. The right panel in Fig.10 illustrates the F_{DF}/F_{grav} trend, showing that for this Event 2 the peaks of the contribution of the DF on BH_{sat} usually take place in correspondence of the minimum distance between the two BHs: as BH_{sat} approaches BH_{cen}, it crosses the central region where the density of stellar particles is higher, thus leading to an increase of the DF acting on it. On the other hand, the DF acting on BH_{cen} is relatively stronger during all the duration of the event, consistent with the the more central position that it occupies.

6.3. Event 3

Finally, the bottom rows of Fig. 9 and of Fig. 10 show the evolution during the Event 3. In this case, at the lower redshift reached by restarting the simulations at $z = 1.26$ to $z = 0.96$, the mass of BH_{cen} is more than 300 times higher than that of BH_{sat}. The latter is initially revolving around the central BH with large oscillations of approximately 30 kpc in amplitude. Once again, REPOS allows the two BHs, initially displaced by 10 kpc, to merge nearly instantaneously, with a "long-range teleporting" of BH_{sat} from the outskirt to the center of the substructure, reported in the top-right inset in the bottom left panel of Fig. 9. Numerical details of the repositioning scheme can affect the amplitude of the jump: its size could be smaller should different or additional constraints be taken into account (e.g. Ragone-Figueroa et al. 2018, as also discussed in Sect. 2.2.1).

Distance oscillation in DYNFRIC, DYNMASS, and NOCORR nearly coincide with each other. However, while DYNFRIC and NOCORR enable the merger to occur after a short time, this does not happen for DYNMASS. The reason for this lies in the different ways in which these simulations match the merging conditions: the distance threshold criterion is satisfied by all three simulations, but the gravitational binding criterion remains unsatisfied for the DYNMASS simulation. BH_{sat}, having its dynamical mass boosted, keeps revolving around BH_{cen} performing wide oscillations of 30 kpc in amplitude. In any case, the similarity of the oscillations described by DYNFRIC and NOCORR suggests that the DF correction in the former should be subdominant in this case. The orbits of BH_{sat} further demonstrate that DYNFRIC, DYNMASS and NOCORR produce almost identical results until $z \simeq 1.1$. In the DYNMASS simulation, the subsequent oscillations of the BH seem to be results of "kicks" that BH_{sat} receives while crossing the denser core of the sub-halo. In the right panel, we note that F_{df}/F_{grav} for BH_{sat} oscillates in phase with the distance between the BHs. We verified that this feature is driven by wide oscillations of the gravitational force, that increases when approaching the galactic core where BH_{cen} resides. Furthermore, the value of F_{df}/F_{grav} for BH_{cen} is significantly higher than for BH_{sat}. This happens both because of the higher mass of the central BH and due to the strong DF correction due to the concentration of stellar particles in the central sub-halo region.

In summary, these three events highlight the importance of adding a correction to the gravitational force onto BHs contributed by the unresolved DF, as demonstrated by Sect. 6.2. Furthermore, the description of such examples of merging events also reveals the significant limitations in correctly describing the dynamics of a system of two BHs of both the REPOS (in the worst-case scenario considered here) and the DYNMASS schemes. Indeed, our simulations based on REPOS generate "jumps" of the BHs, while DYNMASS, by artificially boosting the BH mass, produces two-body scattering effects, preventing the formation of a bound system.

7. Conclusions

We introduced a novel approach to partially correct for the effect of unresolved dynamical friction (DF) on the orbits of black hole (BH) particles in cosmological hydrodynamical simulations. We implemented it in the OpenGadget3 code. The main motivation for this study is to introduce a more physically motivated method to prevent BH particles in simulations to spuriously leave the host galaxies, as a result of finite numerical resolution, and to improve the description of BH-BH mergers. This DF correction has been extensively tested both in zoom-in and fully-cosmological simulations. Specifically, we ran two zoom-in simulations, one for a group-sized and another for a cluster-sized halo, and a cosmological volume having a box size of 16 $cMpc^3$.

We assessed the new model's performance for unresolved DF by carrying out each simulation with other prescriptions for the BH dynamics: the repositioning scheme and the adoption of a large dynamical mass to reinforce the unresolved DF contribution. To sort out the effect of variations in the prescription for BHs dynamics, all simulations were run with identical resolution and sub-resolution physics.

We summarize here below the main conclusions of our analysis.

- **Offset**: The simulations using the continuous repositioning of BH particles on the local potential minimum (REPOS scheme) exhibit the smallest offset between BHs and host sub-halo centers. Our model to correct unresolved DF (DYNFRIC scheme) provides an accurate centering, even outperforming at $z < 1$ the scheme based on boosting the dynamical mass of BH particles at seeding (DYNMASS scheme). See Sect.5.1 and Fig.1.
- **Wandering BHs**: The DYNFRIC simulations produce the smallest population of wandering BHs, which are predominantly found in multiple BH systems. The REPOS prescription features the most numerous and massive set of wandering BHs, as close encounters between galaxies and large-scale potential environments favour the spurious repositioning of BHs outside their host sub-halos. See Sect.5.2, Fig.2, Fig.3 and Fig.4.
- **Mergers**: The overestimate of merger events in the REPOS simulations in denser environment leads to an excess of galaxies deprived of the central BH, an effect that is more pronounced in the denser environment of a massive galaxy cluster. See Sect. 3.2.3, Fig. 5 and Fig. 4.
- **$M_* - M_{BH}$ relation**: The good agreement with the observational data in reproducing the observed $M_* - M_{BH}$ scaling relation in all the simulations demonstrates a relative insensitivity of this diagnostic to the particular prescription adopted,

while it is sensitive to the choice of the parameters regulating BH accretions and the ensuing AGN feedback efficiency. See Sect. 5.4 and Fig. 7.

To delve deeper in the details of how different prescriptions affect the orbits of BH particles, we focused on specific events of BH-BH interactions. To disentangle the possible diversity in the substructure evolution between different simulations, we restarted the simulations from two snapshots of the group-sized halo at $z = 3$ and at $z = 1.26$ to explore how BHs respond to different methodologies governing their dynamics in the same environment. In this analysis, we also carried out simulations without any sub-resolution prescription to correct the orbits of BH particles. The results of this further analysis, introduced in Sect. 6, Fig. 9 and Fig. 10, are summarized here below.

- **DF**: Our novel model to correct DF predicts dumped orbits of the satellite BHs, which gradually approach the center of a host galaxy, thus gently driving to the formation of a close BH-BH pair.
- **Dynamical mass**: The large BH dynamical masses in the `DYNMASS` scheme can lead to spuriously strong interactions between BHs, which could delay or even prevent merging events. In fact, such interactions eventually inhibit the BHs from satisfying the gravitational boundedness criteria for merging. The overall results in terms of correct description of orbit decay in BH pairs can be worse than those obtained without any prescription to correct BH dynamics for unresolved DF.
- **Repositioning**: Our implementation of the `REPOS` method allows for extremely rapid mergers, preceded by large and sudden movements of the satellite BH, that promptly reaches the central region of the sub-halo with few "jumps", that can eventually span several kpcs.

In summary, an extensive analysis of the BH population arising in different simulations demonstrates that our novel implementation of the correction for unresolved DF force acting on BH particles introduced in this paper, provides a robust and reliable description of the DF exerted on BHs by their surroundings. This model reaches at least the same performances of other ad-hoc numerical prescriptions in terms of centering BH in their host halos, while sensibly reducing the population of wandering BHs, and overcoming the limitations of such prescription in the description of BH-BH merger events. Thanks to the recent work by Sala et al. (2023), the `OpenGadget3` code is now equipped with a spin-evolution model that coupled to the DF correction can rely on a more precise description of BH dynamics. Also, the introduction of a DF model is crucial for further investigations on the BH merger rates from cosmological hydrodynamical simulations (e.g. DeGraf et al. 2024), serving as a powerful tool to fully exploit the new window offered by gravitational wave astrophysics.

Acknowledgements. We thank Gian Luigi Granato for a number of useful discussions and comments on this paper, that contributed to improve the presentation of the results. Simulations have been carried out at the CINECA Supercomputing Center (Bologna, Italy), with computing time assigned through ISCRA-B calls and through CINECA-INAF and CINECA-UNITS agreements, and at the computing center of INAF – Astronomical Observatory of Trieste (Bertocco et al. 2020; Taffoni et al. 2020). We acknowledge the CINECA award under the ISCRA initiative, for the availability of high-performance computing resources and support. This paper is supported by: the Italian Research Center on High Performance Computing Big Data and Quantum Computing (ICSC), project funded by European Union - NextGenerationEU - and National Recovery and Resilience Plan (NRRP) - Mission 4 Component 2, within the activities of Spoke 3, Astrophysics and Cosmos Observations; by the PRIN 2022 PNRR project (202259YAF) "Space-based cosmology with Euclid: the role of High-Performance Computing", and by a INAF Grant within the "Astrofisica Fondamentale" funding scheme. We acknowledge partial financial support from the INFN Indark Grant and by the INAF project "CONNECTIONS" (COllaboratioN oN codE development for future Cosmological simulaTIONS). Klaus Dolag acknowledges support by the COMPLEX project from the European Research Council (ERC) under the European Union's Horizon 2020 research and innovation program grant agreement ERC-2019-AdG 882679 as well as support by the Deutsche Forschungsgemeinschaft (DFG, German Research Foundation) under Germany's Excellence Strategy - EXC-2094 - 390783311 We acknowledge the European Union's HORIZON-MSCA-2021-SE-01 Research and Innovation programme under the Marie Sklodowska-Curie grant agreement number 101086388 - Project acronym: LACEGAL.

References

Bahé , Y. M., Schaye, J., Schaller, M., et al. 2022, Monthly Notices of the Royal Astronomical Society, 516, 167
Bassini, L., Rasia, E., Borgani, S., et al. 2020, A&A, 642, A37
Bassini, L., Rasia, E., Borgani, S., et al. 2019, A&A, 630, A144
Beck, A. M., Murante, G., Arth, A., et al. 2016, MNRAS, 455, 2110
Begelman, M. C., Blandford, R. D., & Rees, M. J. 1980, Nature, 287, 307
Bellovary, J. M., Cleary, C. E., Munshi, F., et al. 2018, Monthly Notices of the Royal Astronomical Society
Bertocco, S., Goz, D., Tornatore, L., et al. 2020, in Astronomical Society of the Pacific Conference Series, Vol. 527, Astronomical Data Analysis Software and Systems XXIX, ed. R. Pizzo, E. R. Deul, J. D. Mol, J. de Plaa, & H. Verkouter, 303
Binney, J. & Tremaine, S. 2008, Galactic Dynamics: Second Edition
Bird, S., Ni, Y., Matteo, T. D., et al. 2022, Monthly Notices of the Royal Astronomical Society, 512, 3703
Bonafede, A., Dolag, K., Stasyszyn, F., Murante, G., & Borgani, S. 2011, Monthly Notices of the Royal Astronomical Society, 418, 2234
Bondi, H. 1952, MNRAS, 112, 195
Bondi, H. & Hoyle, F. 1944, MNRAS, 104, 273
Booth, C. & Schaye, J. 2009, Monthly Notices of the Royal Astronomical Society, 398, 53
Borgani, S. & Kravtsov, A. 2011, Advanced Science Letters, 4, 204
Bower, R. G., Benson, A. J., Malbon, R., et al. 2006, MNRAS, 370, 645
Bromm, V. & Loeb, A. 2003, ApJ, 596, 34
Cattaneo, A., Faber, S. M., Binney, J., et al. 2009, Nature, 460, 213, arXiv:0907.1608 [astro-ph]
Chandrasekhar, S. 1943, ApJ, 97, 255
Chen, N., Ni, Y., Tremmel, M., et al. 2022, MNRAS, 510, 531
Combes, F., García-Burillo, S., Audibert, A., et al. 2019, A&A, 623, A79
Davé, R., Anglés-Alcázar, D., Narayanan, D., et al. 2019, Monthly Notices of the Royal Astronomical Society, 486, 2827
DeBuhr, J., Quataert, E., & Ma, C.-P. 2011, Monthly Notices of the Royal Astronomical Society, 420, 2221
DeGraf, C., Chen, N., Ni, Y., et al. 2024, MNRAS, 527, 11766
Di Matteo, Daniel Angles-Alcazar, F. S. 2023 [arXiv:2304.11541]
Di Matteo, T., Colberg, J., Springel, V., Hernquist, L., & Sijacki, D. 2008, ApJ, 676, 33
Dolag, K., Borgani, S., Murante, G., & Springel, V. 2009, MNRAS, 399, 497
Dubois, Y., Volonteri, M., & Silk, J. 2014, Monthly Notices of the Royal Astronomical Society, 440, 1590–1606
Eke, V. R., Cole, S., Frenk, C. S., & Navarro, J. F. 1996, MNRAS, 281, 703
Fabjan, D., Borgani, S., Tornatore, L., et al. 2010, MNRAS, 401, 1670
Fabjan, D., Borgani, S., Tornatore, L., et al. 2010, Monthly Notices of the Royal Astronomical Society, 401, 1670
Ferrarese, L. & Merritt, D. 2000, The Astrophysical Journal, 539, L9, arXiv:astro-ph/0006053
Ferrarese, L., Pogge, R. W., Peterson, B. M., et al. 2001, Supermassive Black Holes in Active Galactic Nuclei. I. The Consistency of Black Hole Masses in Quiescent and Active Galaxies, arXiv:astro-ph/0104380
Gaspari, M., Eckert, D., Ettori, S., et al. 2019, The Astrophysical Journal, 884, 169, arXiv:1904.10972 [astro-ph, physics:physics]
Gebhardt, K., Bender, R., Bower, G., et al. 2000, The Astrophysical Journal, 539, L13, arXiv:astro-ph/0006289
Gitti, M., Brighenti, F., & McNamara, B. R. 2012, Advances in Astronomy, 2012, 1
Graham, A. W. & Driver, S. P. 2007, The Astrophysical Journal, 655, 77, arXiv:astro-ph/0607378
Granato, G. L., De Zotti, G., Silva, L., Bressan, A., & Danese, L. 2004, ApJ, 600, 580
Groth, F., Steinwandel, U. P., Valentini, M., & Dolag, K. 2023, arXiv e-prints, arXiv:2301.03612

Gultekin, K., Richstone, D. O., Gebhardt, K., et al. 2009, The M-sigma and M-L Relations in Galactic Bulges and Determinations of their Intrinsic Scatter, arXiv:0903.4897 [astro-ph]
Haering, N. & Rix, H.-W. 2004, The Astrophysical Journal, 604, L89, arXiv:astro-ph/0402376
Hirschmann, M., Dolag, K., Saro, A., et al. 2014, Monthly Notices of the Royal Astronomical Society, 442, 2304
Hopkins, P. F., Hernquist, L., Cox, T. J., et al. 2005, A Unified, Merger-Driven Model for the Origin of Starbursts, Quasars, the Cosmic X-Ray Background, Supermassive Black Holes and Galaxy Spheroids, arXiv:astro-ph/0506398
Hoyle, F. & Lyttleton, R. A. 1939, Proceedings of the Cambridge Philosophical Society, 35, 405
Kormendy, J., Beckman, J., Colina, L., & Netzer, H. 1993, Consejo Superior de Investigaciones Cientificas (Madrid, 1993)
Ma, L., Hopkins, P. F., Kelley, L. Z., & Faucher-Giguère, C.-A. 2023, Monthly Notices of the Royal Astronomical Society, 519, 5543
Magorrian, J., Tremaine, S., Richstone, D., et al. 1998, The Astronomical Journal, 115, 2285, arXiv:astro-ph/9708072
Mayer, L. & Bonoli, S. 2018, Reports on Progress in Physics, 82, 016901
McConnell, N. J. & Ma, C.-P. 2013, The Astrophysical Journal, 764, 184, arXiv:1211.2816 [astro-ph]
Menezes, R. B., Steiner, J. E., & Ricci, T. V. 2014, The Astrophysical Journal, 796, L13
Merritt, D. & Ferrarese, L. 2000, The M(BH)-Sigma Relation for Supermassive Black Holes, arXiv:astro-ph/0008310
Noble, S. C., Krolik, J. H., Schnittman, J. D., & Hawley, J. F. 2011, The Astrophysical Journal, 743, 115
Novikov, I. D. & Thorne, K. S. 1973, Black holes (Les astres occlus), 1, 343
Ostriker, E. C. 1999, The Astrophysical Journal, 513, 252
Pfister, H., Volonteri, M., Dubois, Y., Dotti, M., & Colpi, M. 2019, Monthly Notices of the Royal Astronomical Society, 486, 101
Pillepich, A., Springel, V., Nelson, D., et al. 2017, Monthly Notices of the Royal Astronomical Society, 473, 4077
Ragagnin, A., Dolag, K., Wagner, M., et al. 2020, arXiv e-prints, arXiv:2003.10850
Ragagnin, A., Tchipev, N., Bader, M., Dolag, K., & Hammer, N. J. 2016, in Advances in Parallel Computing, 411–420
Ragone-Figueroa, C., Granato, G. L., Ferraro, M. E., et al. 2018, Monthly Notices of the Royal Astronomical Society
Ragone-Figueroa, C., Granato, G. L., Murante, G., Borgani, S., & Cui, W. 2013, MNRAS, 436, 1750
Reines, A. E., Condon, J. J., Darling, J., & Greene, J. E. 2020, The Astrophysical Journal, 888, 36
Sala, L., Valentini, M., Biffi, V., & Dolag, K. 2023, Supermassive black hole spin evolution in cosmological simulations with OpenGadget3
Schaye, J., Crain, R. A., Bower, R. G., et al. 2014, Monthly Notices of the Royal Astronomical Society, 446, 521
Sijacki, D. & Springel, V. 2006, Monthly Notices of the Royal Astronomical Society, 366, 397
Sijacki, D., Vogelsberger, M., Genel, S., et al. 2015, Monthly Notices of the Royal Astronomical Society, 452, 575
Silk, J. & Rees, M. J. 1998, Quasars and Galaxy Formation, arXiv:astro-ph/9801013
Springel, V. 2005, Monthly Notices of the Royal Astronomical Society, 364, 1105
Springel, V. 2016, in Saas-Fee Advanced Course, Vol. 43, Saas-Fee Advanced Course, ed. Y. Revaz, P. Jablonka, R. Teyssier, & L. Mayer, 251
Springel, V., Di Matteo, T., & Hernquist, L. 2005a, Monthly Notices of the Royal Astronomical Society, 361, 776
Springel, V. & Hernquist, L. 2003, MNRAS, 339, 289
Springel, V., Matteo, T. D., & Hernquist, L. 2005b, Monthly Notices of the Royal Astronomical Society, 361, 776
Springel, V., White, S. D. M., Tormen, G., & Kauffmann, G. 2001a, MNRAS, 328, 726
Springel, V., White, S. D. M., Tormen, G., & Kauffmann, G. 2001b, MNRAS, 328, 726
Steinborn, L. K., Dolag, K., Hirschmann, M., Prieto, M. A., & Remus, R.-S. 2015, MNRAS, 448, 1504
Taffoni, G., Becciani, U., Garilli, B., et al. 2020, in Astronomical Society of the Pacific Conference Series, Vol. 527, Astronomical Data Analysis Software and Systems XXIX, ed. R. Pizzo, E. R. Deul, J. D. Mol, J. de Plaa, & H. Verkouter, 307
Teyssier, R. 2002, A&A, 385, 337
Tornatore, L., Borgani, S., Dolag, K., & Matteucci, F. 2007, MNRAS, 382, 1050
Tremmel, M., Governato, F., Volonteri, M., & Quinn, T. R. 2015, Monthly Notices of the Royal Astronomical Society, 451, 1868
Vogelsberger, M., Genel, S., Sijacki, D., et al. 2013, Monthly Notices of the Royal Astronomical Society, 436, 3031
Volonteri, M. & Bellovary, J. 2012, Reports on Progress in Physics, 75, 124901
Webb, N., Cseh, D., Lenc, E., et al. 2012, Science, 337, 554
Wiersma, R. P. C., Schaye, J., & Smith, B. D. 2009, MNRAS, 393, 99
Wurster, J. & Thacker, R. J. 2013, Monthly Notices of the Royal Astronomical Society, 431, 2513